Research Square

Preprints are preliminary reports that have not undergone peer review.
They should not be considered conclusive, used to inform clinical practice,
or referenced by the media as validated information.

Topology-Optimized 3D Infill Generation Using the Ground Structure Method for Material Extrusion Additive Manufacturing

Shadman Tajwar Shahid

sshahid@mtech.edu

Military Institute of Science and Technology

Md. Mahidul Alam

Military Institute of Science and Technology

Research Article

Keywords: Topology Optimization, Finite Element Analysis, Ground Structure Method, Fused Deposition Modelling, Closed Cell Lattice, Skin-Lattice Structure

Posted Date: April 7th, 2026

DOI: https://doi.org/10.21203/rs.3.rs-9323486/v1

License: This work is licensed under a Creative Commons Attribution 4.0 International License.
Read Full License

Additional Declarations: The authors declare no competing interests.

Topology-Optimized 3D Infill Generation Using the Ground Structure Method for Material Extrusion Additive Manufacturing

Shadman Tajwar Shahid[a,*], Md. Mahidul Alam[a], Mahmudul Hasan[a], Md. Rakidul Islam[a], Shah Md. Ahasan Siddique[a]

[a] Department of Mechanical Engineering, Military Institute of Science and Technology, Mirpur Cantonment, Dhaka-1216, Bangladesh

Corresponding author name and address: Shadman Tajwar Shahid, Department of Mechanical Engineering, Military Institute of Science and Technology, Mirpur Cantonment, Dhaka-1216, Bangladesh.
Email: shadmantajwar@me.mist.ac.bd

Abstract: This paper presents a Ground Structure Method (GSM)-based topology optimization framework to create optimized 3D infill structures tailored to material extrusion additive manufacturing. The infill is considered a closed lattice structure and modeled as a pin-jointed truss. Multiple meshing techniques are investigated to embed the lattice within an arbitrary geometry, producing a skin-lattice structure that serves as both the Finite Element Analysis (FEA) mesh and the infill geometry. A size optimization algorithm based on the Method of Moving Asymptotes (MMA) adjusts strut thicknesses to maximize rigidity. To translate the optimized structure into a printable form, a rasterization-based slicer is introduced, which directly converts the intersections between slicing planes and the FEA mesh into 2D bitmaps, with the contour at each layer mapped to the optimized truss thicknesses. Lastly, an image-to-toolpath process automatically generates the machine files from bitmaps. The method's generality is demonstrated through numerical simulations and printed examples for both 2D and 3D cases. Additionally, experiments show an improvement in stiffness of topology-optimized structures compared to uniform infill structures.

Keywords: Topology Optimization, Finite Element Analysis, Ground Structure Method, Fused Deposition Modelling, Closed Cell Lattice, Skin-Lattice Structure.

1. Introduction

Additive manufacturing (AM) allows the fabrication of objects of highly complex external and internal geometries. Among the various AM processes, the most widely adopted is the hot wire deposition technique, commonly known as Fused Deposition Modeling (FDM) or Fused Filament Fabrication (FFF) [1, 2]. Slicing software typically creates outer walls that define the object's contour, providing shape and structural integrity. The internal volume is filled with a porous infill structure, such as a cellular or lattice configuration, rather than a completely solid volume [3, 4]. These infill designs are generated based on equation-driven patterns with a specific volume fraction, and several studies have investigated their influence on mechanical strength [5-7]. However, these infills are distributed uniformly throughout the parts and, therefore, are not an optimal design since not all regions undergo the same mechanical stress during loading [8, 9].

Topology optimization (TO) is a mathematical method to optimize the material distribution within a specific design volume [10]. Topology-optimized structures are typically characterized by complex geometric configurations that are challenging to manufacture using conventional processes. In this context, AM opens the possibility of manufacturing topology-optimized structures without additional tools, molds, and processes [11].

The current research on TO, which takes advantage of AM, mainly concentrates on two aspects: one is to design high-performance additively manufactured multi-scale/multi-hierarchical structures, and the other is to integrate AM design constraints into TO to achieve product design and manufacturing integration [12, 13]. In recent years, the optimization design of multi-scale or hierarchical lattice structure has been a widely investigated field in the integration of TO and includes: (1) Design of hierarchical structure by mapping with density-based TO method [14-21], (2) concurrent optimization of macrostructure and microstructure [22-32], and (3) design of hierarchical structure based on strut sizing operation [33-38].

In a density-based hierarchical structure design, the design volume is treated as a continuous material with a homogenized property. Instead of optimizing each lattice element individually, the method assumes that the material behaves as a continuum. Thereafter, TO is conducted, and the optimum density distribution is mapped into the construction of the lattice structure [14, 15]. Panesar et al. presented several strategies to derive the lattice structure from SIMP (solid isotropic material with penalization) TO results [16]. The relative density mapping (RDM) method proposed

by Alzahrani et al. uses the relative density information from FEA in designing 3D lattice structures [17]. Aremu et al. presented a voxel-based method of generating lattices comprised of any cell type that can conform to an arbitrary external geometry [18]. The voxel representation of the structure considers matrices of ones and zeros to represent the presence and absence of material, respectively, and the method can also generate functionally graded structures. Xiao et al. propose a gradient-based approach to optimizing the shape and infill of lattice-skin structures to improve their efficiency [19]. Here, the lattice was modeled as a pin-jointed truss structure, and a penalization approach akin to the SIMP method was used for TO of the lattice. Similarly, Wang et al. proposed a method for generating self-supporting lattice structures within a TO framework [20]. Liu et al. proposed a generative strategy for lattice infill generation using organic strut-based lattices, where a sphere packing algorithm driven by a Von Mises stress field determined the lattice distribution density [21].

Another approach to hierarchical structure is the multi-scale concurrent TO of structures, which bridges both macrostructures and microstructures to obtain higher performance schemes [22]. A common objective of these works is to improve the manufacturability of topology-optimized parts using lattice structures to support the solid overhangs [23-25]. Rodrigues et al. proposed a hierarchical computational procedure for optimizing material distribution and local microstructures [26]. Coelho et al. extended this work to three-dimensional structures [27]. Wang et al. [28] present a two-scale concurrent TO approach via homogenization for finding the optimum topology of macrostructures and their corresponding material microstructures. Furthermore, various TO methods such as Bidirectional Evolutionary Structural Optimization (BESO) [29-31], and moving iso-surface threshold method (MIST) [32] are applied for the design of solid lattice hybrid structures.

The other widely adopted strategy for designing lattice structures is by strut sizing operation using the ground structure method (GSM). The method starts with a predefined network of potential truss elements—nodes interconnected by a dense set of struts within the design volume. The optimal structure is obtained by selecting an optimal substructure from this network. The GSM is essentially a sizing optimization problem where member cross-sectional areas are the design variables [33-35]. Based on the GSM, Chen et al. proposed a parametrized modelling and optimization method for generating non-uniform lattice structures [36]. Ohsaki et al. [37, 38]

presented a method for simultaneously optimizing the geometry and topology of plane and spatial trusses, considering force density as the design variable. Huang et al. [39] presented a GSM approach of TO accounting for the manufacturing constraint of uniform cross-section and average member length. Moreover, a robotic AM framework of the 3D topology-optimized truss structure is demonstrated. Given the literature on topology optimization and the design freedom afforded by AM to fabricate complex lattice structures, there is potential to design a structurally optimized infill of a part whilst maintaining the external form.

Thus, this paper proposes a method for generating a topology-optimized infill structure. The infill structures are considered closed lattice structures, and in this work, the terms “infill structure” and “lattice structure” are used interchangeably. The lattice is modeled as a pin-jointed truss structure, and the GSM of parametrization and optimization for truss structures is used. Unlike density-based methods, where the strut sizes of the lattice are mapped to the results of TO, GSM optimizes the strut sizes directly; thus, mapping is not needed. Moreover, in density-based methods, the optimized lattice structure is optimal only when the structure consists of periodically patterned microstructures of infinitesimal size, i.e., a continuum solid with embedded microstructures. So, the GSM approach becomes appropriate when individual element sizes are comparable to the length scale of the global structure, such as when using an infill of a lower infill percentage or large-scale lattice structures.

While shell-lattice or skin-lattice structures have been widely studied using density-based and implicit topology optimization methods, these methods fundamentally differ from the GSM. In contrast to these continuum-based approaches, the Ground Structure Method (GSM) operates directly on discrete strut elements. Although the GSM has been widely applied in 2D structural optimization, its extension to 3D domains has been limited due to the presence of geometric artifacts, specifically weak, floating struts along the domain boundaries [24, 38-40]. These floating struts introduce unconstrained degrees of freedom, resulting in singular stiffness matrices and numerical failure.

Existing 3D GSM implementations, such as the GRAND3 framework [40], use a subtractive geometric filtering approach to handle arbitrary shapes. In this method. a dense 3d ground structure is “cropped” to fit the domain. Any members intersecting the boundary or hole are deleted. This subtractive process fundamentally alters the original geometry of the structure. Furthermore, recent

3D GSM advancements [24, 39] primarily generate open-frame spatial lattices that lack a functional exterior surface.

In contrast, the proposed method introduces a coupled shell-lattice framework. Rather than treating the 3D design domain as a passive filter, we use a “net-skin” coupling method. This approach inherently connects all exterior and potentially loose lattice struts to the shell, effectively "anchoring" the ground structure instead of cropping it. This eliminates the possibility of boundary-related instabilities during optimization and gives a GSM framework that maintains strict geometric similarity to the original design domain.

In addition, the conversion from an optimized structure to printable files presents a significant challenge for 3D lattices. Most existing lattice-optimization workflows for FDM require exporting an intermediate geometry file before toolpath generation, a step that is often unreliable for complex lattice structures [18]. The proposed method departs from this convention by rasterizing the optimized GSM lattice directly into per-layer 2D bitmaps and extracting FDM-ready extruder paths from these bitmaps. This creates a more reliable and direct pathway from structural optimization to fabrication.

The remainder of this paper is organized as follows: Section 2 details the proposed methodology, including mesh generation, topology optimization, rasterization, and extruder path generation. Section 3 presents the computational studies and experimental validation. Finally, Section 4 concludes the paper with a discussion of potential future research directions.

2. Methodology

The objective is to create topology-optimized infill, taking into consideration the manufacturing constraints of FDM AM. The method retains the outer shape of the object while maintaining dimensional accuracy, and can be applied to complex 2D and 3D geometries. The implementation is fully carried out in Python due to its ease of automation and integration of topology optimization (TO) workflows with machine file generation.

The first step is the construction of the part in stereolithography (STL) format, referred to as the design STL or domain in this work. The second step is to generate the FEA mesh by embedding the interior of the design STL file with a lattice structure that forms the shape of the infill and is also used for finite element analysis (FEA). A parametric description of the mesh is generated

based on vertex positions and edges, and the boundary conditions are applied. The third step is to solve for the optimized size of the struts of the mesh using the results of FEA by the method of moving asymptotes (MMA). In the fourth step, slicing planes are generated, and the intersection between the planes and the FEA mesh is identified. The intersections are converted to 2D bitmaps where the intersections are drawn as wide lines, the width corresponding to the optimized strut thickness. The fifth step is generating extruder paths from the 2D bitmaps, which involves contour extraction, smoothing, ordering, hole identification, and calculating offset paths. Finally, machine files are created from the extruder paths. The overall workflow for topology-optimized 3D infill generation is shown in Figure 1.

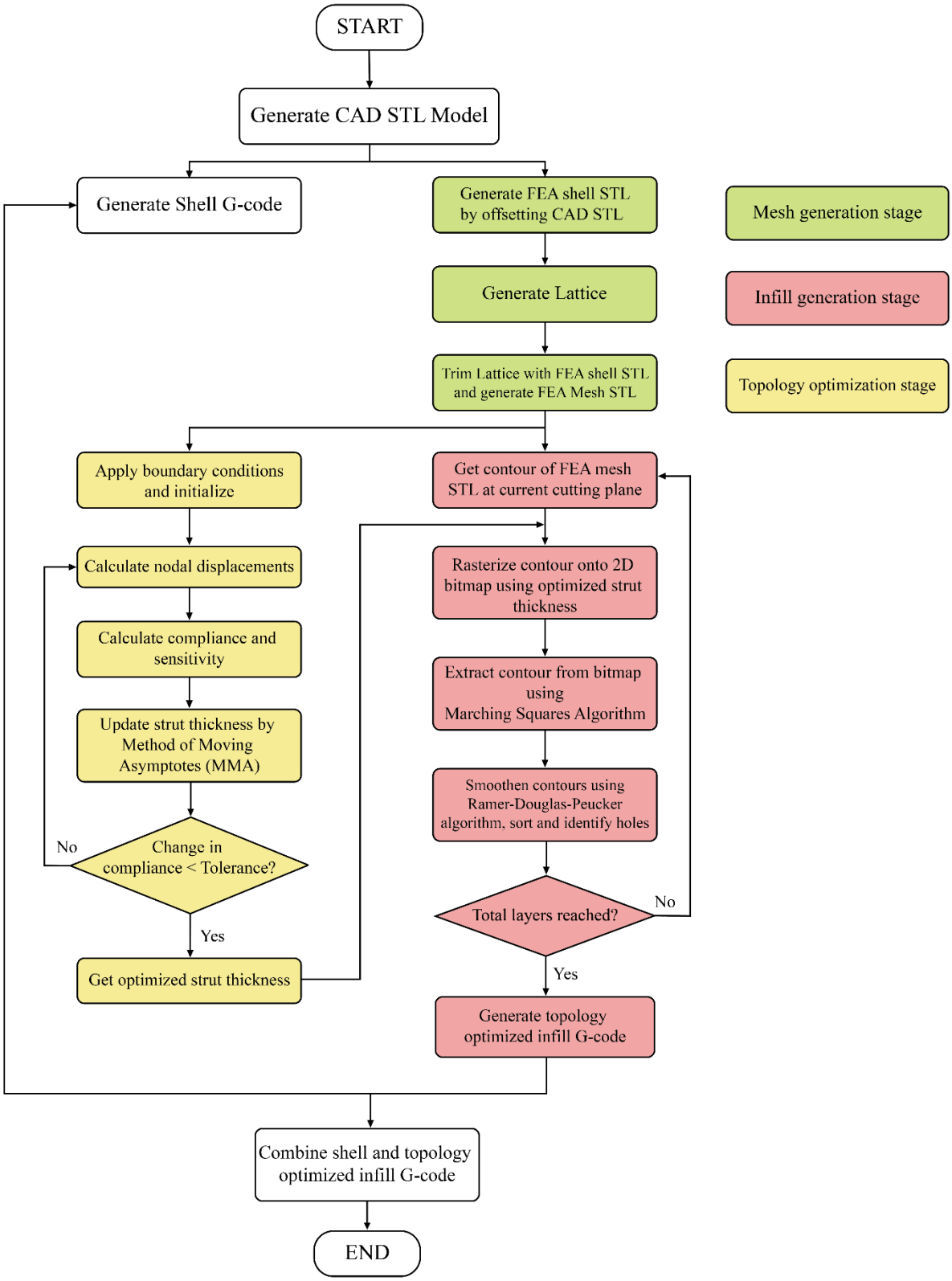


Fig. 1. Topology optimized 3D infill generation workflow.

2.1. Meshing

Finite element analysis (FEA) is based on the decomposition of a continuum into a finite number of discrete elements called a mesh, the solution being an approximation of the exact solution [41]. In this work, the mesh serves a dual purpose: it is used in the FEA stage during TO, and it is also used to define the lattice shape, with the edges of the FEA mesh serving as struts of the lattice structure.

2.1.1. 2D Meshing

For arbitrary shapes, it is desirable that the lattice structure conforms to the outer boundary. Moreover, the structural properties of the structures depend on the unit cell and the meshing techniques used. For 2D mesh generation, three different techniques were evaluated: (i) the lattice is swept to fit the domain; (ii) by using meshing schemes of FEA software; and (iii) by using the domain to trim a tessellated lattice structure, as seen in Figure 2.

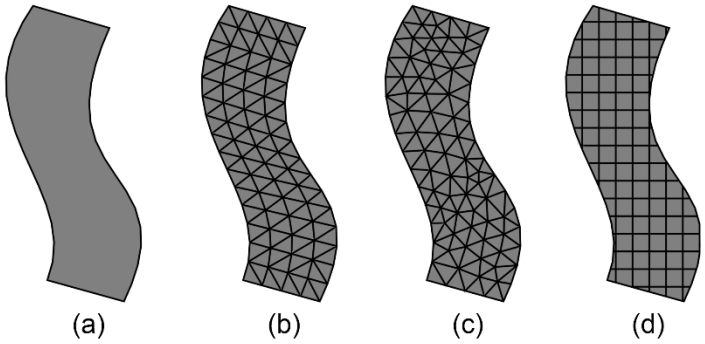


Fig. 2. 2D mesh generation methods: a) domain, b) swept, c) meshed, d) trimmed.

In a swept lattice structure, the unit cell aligns with the boundaries of the domain. Such conformal lattice structures are stronger and stiffer per unit mass than uniform lattice structures [18, 42, 43]. However, the construction of such structures is limited by the simple patterning operations in commercial geometric modeling packages. Complex domains take manual construction, which is not always feasible due to the large number of struts in a typical lattice structure.

Figure 2(c) shows a lattice generated by meshing schemes available in FEA software. The field of FEA is well established, and sophisticated meshing algorithms are used to discretize a domain before analysis [44]. However, a limitation in this method is that the structure will be distorted, and there is limited control over the shape of the unit cell [18].

Trimming the tessellated lattice with the domain is a preferable approach if control over the unit cell is to be retained. In this method, a lattice structure is generated to fully encompass the domain, and a Boolean intersection operation is performed to retain only the portion of the lattice that lies within the domain boundary. Following the trimming process, Delaunay triangulation is used to convert any non-triangular faces (n-gons) into triangles.

2.1.2. 3D Meshing

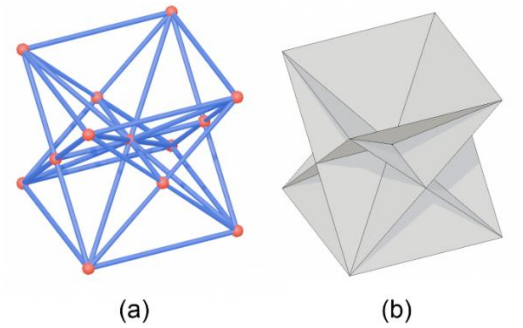


Fig. 3. Unit cell used for lattice structure (a) the nodes are displayed in red; the elements/struts are displayed in blue; (b) the STL representation of the unit cell.

For 3D mesh generation, the trimming technique is evaluated. The shape of the unit cell is crucial, as it determines the mechanical properties of the lattice structure and compliance with FDM-specific constraints. To generate a self-supporting infill structure, the angle between the struts and the printing direction must be larger than the overhang threshold, 45 degrees [18]. Moreover, since the infill is generated by slicing explicitly defined geometry, faces parallel to the printing direction are not printed, as they are not intersected by the slicing planes. The unit cell used in this study is a body-centered cubic and face-centered cubic (BCC and FCC) unit cell with the top and bottom planes removed, as shown in Figure 3. The unit cell was selected based on previous studies, which exhibited high stiffness, buckling resistance, and are less anisotropic compared to other lattice topologies [45-48]. Additionally, this unit cell gives a consistent infill structure, similar in shape to the cubic infill in standard slicers, that the top layers can attach to and bridge across.

The unit cells are guaranteed to be manufacturable by applying a minimum strut size constraint (a_{min}) of 0.4 mm during the optimization stage, which is the minimum extrusion width of the FDM 3D printer used. There is no strict limitation on the unit-cell size. However, small cells may cause adjacent stiff regions to merge during rasterization, effectively forming solid areas rather than

discrete closed-shell structures. Conversely, large unit cells may result in sparse infill, which may be insufficient to support the upper layers.

Manufacturability is strictly enforced by the choice of lattice geometry and strut dimensions, without explicitly including additional AM constraints. While this reduces computational overhead at the optimization level and allows a highly customizable and versatile range of unit-cell geometries to be used, it introduces certain limitations. The formulation is based on classical linear-elastic compliance minimization, which assumes ideal material behavior and perfect bonding between layers. In reality, FDM parts are inherently anisotropic and exhibit non-linear mechanical response or defects that the linear model does not account for.

Moreover, no explicit global AM constraints are integrated into the optimizer. These include geometric constraints, such as layer-wise connectivity and large-scale overhangs, as well as physical constraints like residual thermal stress. The absence of geometric constraints means that if the optimized infill geometry varies drastically between consecutive layers, large-scale overhangs or isolated "islands" may arise that exceed the self-supporting capabilities of the printer. Thus, while the unit cell geometry remains the most significant parameter to ensure manufacturability, the actual structural performance remains sensitive to design domain geometry, specific printer settings, and material properties.

In a conventional open cell lattice structure, the edges of the unit cells are thin tubular struts. However, in FDM, these struts are translated as small, isolated regions in each sliced layer, which are more prone to defects such as layer spacing, material gaps, material bulges, and stringing [11]. Instead of tubular struts, this work uses a thin-walled or closed-cell structure approach where the faces of the lattice are filled with material. Such structures are substantially stiffer and more manufacturable by FDM than open-cell structures, as the extruder follows longer, continuous paths with fewer retractions, resulting in fewer defects [49-52]. So, the faces are retained in the STL representation of the lattice, and material is deposited on the 2D slice of the faces.

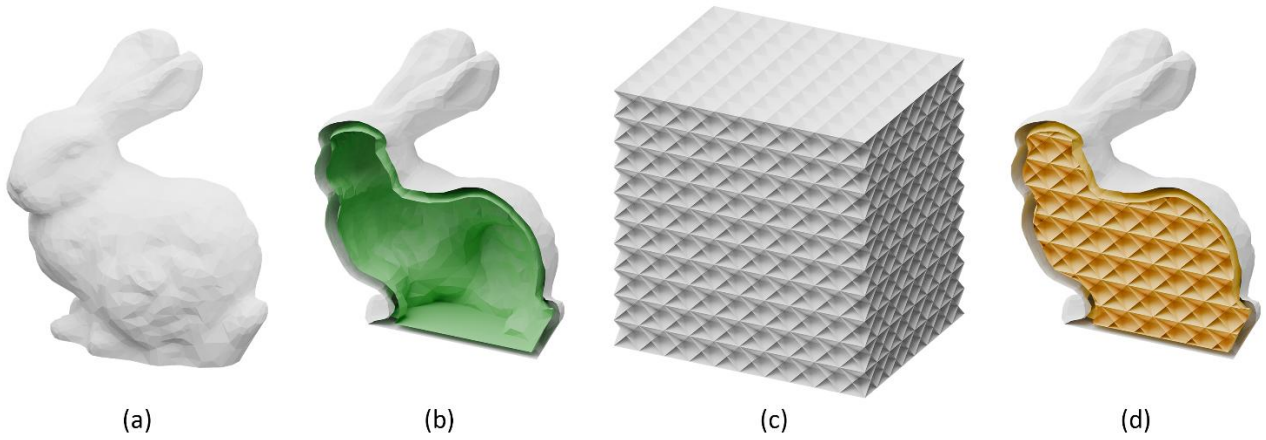


Fig. 4. (a) Design STL model, (b) FEA shell (green) generated by offsetting the design STL model, (c) Lattice structure generated within the bounding box of the design STL model, (d) FEA mesh (yellow) generated after trimming and coupling between the FEA shell and the lattice structure.

The starting point is the geometry that defines the design domain, and a lattice structure that fully encompasses the domain. The design domain and lattice structure are represented using STL files, as they are widely used in commercial modeling packages. The design STL model is offset by a distance depending on the number of walls and extrusion width, so that no material overlaps between the walls and infill [53, 54]. The offset model is referred to as the FEA shell. The internal volume of the domain is initially populated with a lattice structure by a Boolean intersection or trimming operation.

The advantage of the trimming method is that it applies to both simple and complicated cells and domains. However, an artifact of such a trimmed structure is the emergence of weak, unconnected structural features at the trimmed boundaries, which can cause unconstrained rigid body motion and numerical instabilities in the analysis [18].

To resolve these instabilities, a coupling process is performed following the initial trimming. Rather than treating the FEA shell and trimmed lattice as separate entities, a self-intersection algorithm is applied to the combined geometries. This operation creates a coincident vertex at every location where an internal lattice strut terminates at the shell boundary. Merging these coincident vertices anchors the previously floating elements to the exterior skin, resulting in a unified mesh. As a result, the shell will also contribute to the overall structure and subsequently the TO of the infill. The steps of mesh generation are shown in Figure 4.

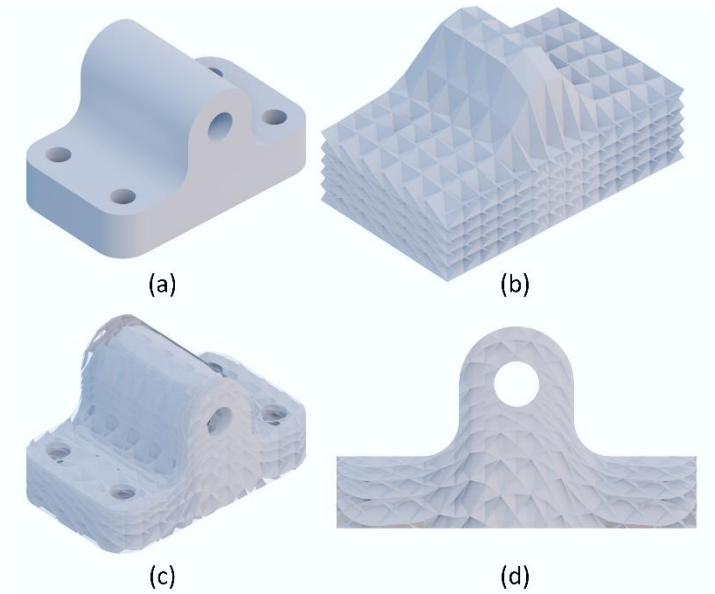


Figure 5. (a) design domain, (b) uniform lattice mapped to the design domain, (c) hybrid-conformal after Boolean intersection with design domain, and (d) side view of the resulting hybrid-conformal structure.

The trimming and coupling-based approach of lattice construction also allows the realization of a hybrid-conformal structure. This can be achieved by mapping the bounding box of the uniform lattice to the top and bottom surfaces of the design domain. Since the mapped lattice may extend outside the domain boundaries, trimming is applied to remove excess. An example of such a hybrid-conformal lattice structure is shown in Figure 5. In the present work, conformality of the lattice is not attempted, and the scope is limited to a uniform lattice. Nevertheless, topology optimization of a hybrid-conformal lattice has the potential to achieve improved mechanical performance, as struts better aligned with the applied loads can improve load transfer and promote stretching-dominated behavior.

Although the lattice is represented as a closed-cell structure in the geometric model, it is treated as a pin-jointed truss during optimization, where the edges of the triangular faces are used as struts. This approximation neglects the bending and shear stiffness contributions of the thin-walled faces of the closed-cell lattice. Previous studies have shown that printed closed-cell lattice structures of the unit cell used in this work (BCC and FCC with the top and bottom faces removed) exhibit higher plateau and densification stresses than open-cell or pin-jointed counterparts [49,50]. As a result, the pin-jointed optimized structures represent a lower-bound estimate of stiffness and stability.

Since the optimization objective is compliance minimization, which prioritizes the identification of optimal load paths, rather than absolute stiffness prediction, the pin-jointed representation yields reliable topology layouts that are qualitatively consistent with more computationally expensive shell-based models. Overall, this modeling choice provides a conservative approximation that simplifies the optimization and avoids overestimating structural performance.

Lastly, a parametric description of the mesh is generated based on the node coordinates and connections. The boundary conditions are applied at the nodes, designating some nodes as having fixed displacements and others as having prescribed loads.

2.2. Finite Element Analysis

The infill lattice structure generated in our method is modeled as a pin-jointed truss structure. Consequently, the finite element analysis (FEA) method, which is commonly used in truss structure analysis, is applicable [55]. FEA uses the stiffness of each element to determine the forces set up in a truss member by calculating the displacement of the nodes. Based on the principle that the sum of forces applied by all the elements connected to a node must equal the forces applied externally to the node, a set of linear algebraic equations is assembled in a matrix form:

$$\begin{bmatrix} K_{11} & K_{12} & \cdots & K_{1n} \\ K_{21} & K_{22} & \dots & K_{2n} \\ \vdots & \vdots & \ddots & \vdots \\ K_{n1} & K_{n2} & \dots & K_{nn} \end{bmatrix} \begin{pmatrix} u_1 \\ u_2 \\ \vdots \\ u_n \end{pmatrix} = \begin{pmatrix} f_1 \\ f_2 \\ \vdots \\ f_n \end{pmatrix} \tag{1}$$

u and f are the deflections and forces at the i_{th} node, respectively. The K coefficient array is called the global stiffness matrix. The i-j component is the contribution of j_{th} displacement on the i_{th} forces.

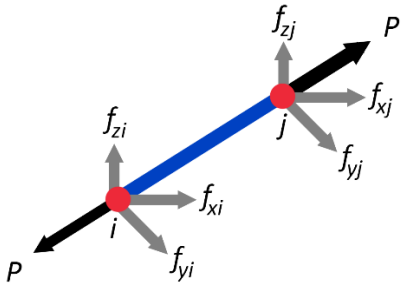


Fig. 6. Components of nodal force. The nodes are displayed in red; the elements/struts are displayed in blue.

To construct the matrix equation that describes the entire truss system, the relationship between forces and displacement at each end of an individual element must be established. In this case, the element is a 3D truss element. For a truss element in 3D space, as shown in Figure 6, connected to nodes *i* and *j*, the nodal force components are given by the equation:

$$\begin{pmatrix} f_{xi} \\ f_{yi} \\ f_{zi} \\ f_{xj} \\ f_{yj} \\ f_{zj} \end{pmatrix} = \frac{AE}{L} \begin{bmatrix} C_x^2 & C_xC_y & C_xC_z & -C_x^2 & -C_xC_y & -C_xC_z \\ C_yC_x & C_y^2 & C_yC_z & -C_yC_x & -C_y^2 & -C_yC_z \\ C_zC_x & C_zC_y & C_z^2 & -C_zC_x & -C_zC_y & -C_z^2 \\ -C_x^2 & -C_xC_y & -C_xC_z & C_x^2 & C_xC_y & C_xC_z \\ -C_yC_x & -C_y^2 & -C_yC_z & C_yC_x & C_y^2 & C_yC_z \\ -C_zC_x & -C_zC_y & -C_z^2 & C_zC_x & C_zC_y & C_z^2 \end{bmatrix} \begin{pmatrix} u_i \\ v_i \\ w_i \\ u_j \\ v_j \\ w_j \end{pmatrix}. \tag{2}$$

where,

$$C_x = \frac{x_j - x_i}{L}, \qquad C_y = \frac{y_j - y_i}{L}, \qquad C_z = \frac{z_j - z_i}{L}. \tag{3}$$

Here, *A*, *E*, and *L* represent the element-wise area, modulus of elasticity, and length, respectively.

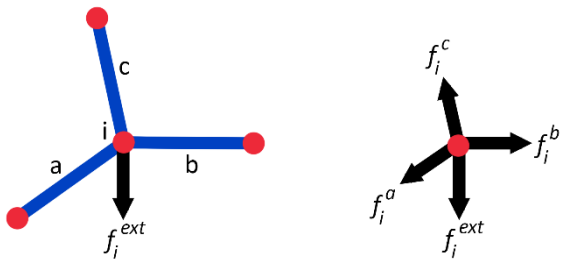


Fig. 7. Element/strut contributions to total nodal force.

Now, considering a node connected by multiple truss elements, as shown in Figure 7. Each element meeting at a node will contribute a force that is dictated by both of that element's nodes. Maintaining static equilibrium, the sum of all the forces contributed by the elements at a given node must equal the forces that are applied externally to the node, so that

$$f_i^{ext} = \sum_{elem} f_i^{elem} = \sum_{elem} k_{ij}^{elem} u_j = (\sum_{elem} k_{ij}^{elem}) u_j = K_{ij} u_j. \tag{4}$$

In the assembly process, the element stiffness matrix of each matrix is added to the appropriate position in the overall, or "global" stiffness matrix that relates all the truss displacements and forces. The equation of the system is derived and solved for the nodal displacements.

2.3. Topology Optimization

The objective of TO in this context is to determine the cross-sectional area of the member or struts in a 3D truss so that the stiffness is maximized. Stiffness is quantified using the compliance C of the truss, which is defined as,

$$C = u_T K u. \tag{5}$$

In a nested formulation, compliance is a convex function of the design variable, the cross-sectional area of the members. In a truss where compliance has been minimized for a given amount of material, all bars will have the same stress, thus making efficient use of available materials [56]. The optimization problem may be written as the following nested formulation:

$$(\mathbb{P})_{sf} \begin{cases} \min\limits_{a} C(\mathrm{a}) \\ s.t. \quad \begin{cases} \mathrm{K(a)\ u\ =\ F}, \\ \sum\limits_{j} l_j a_j \ \le V_{\max}, \\ a_{min} \le a_j \le a_{max}, \qquad \mathrm{j\ =\ 1,\ldots,n.} \end{cases} \end{cases} \tag{6}$$

Where a is the vector of design variables (cross-sectional areas of the bars), l_j is the length of the j-th bar, V_{max} is the maximum allowed volume of the truss, and a_{min} and a_{max} are the lower and upper bounds on the design variables, respectively.

We solve the problem numerically by generating a sequence of explicit, convex approximations using the Method of Moving Asymptotes (MMA) approximation [57, 58]. As inputs, the following information is needed: the coordinates of the nodes, their connections, boundary conditions, the forces applied, Young's modulus E, lower and upper bounds of the design variable, a_{min} and a_{max}, and the maximum allowed volume of the truss, V_{max}. Moreover, the initial design variable a, the values of the lower asymptotes, and the dual variable λ must be initialized.

At each iteration, the FEA is performed to calculate the nodal displacements using the current design variable a. The global stiffness matrix K is assembled, and the equilibrium equation $Ku = F$ is solved. This is the most computationally intensive part of the algorithm.

The objective function, defined as the derivative of compliance with respect to the design variable (known as the sensitivity), is computed as,

$$\frac{\delta C}{\delta a_j} = -u^T \frac{\delta K}{\delta a_j} u. \tag{7}$$

These sensitivities guide the optimization process. To avoid numerical instabilities, a small positive offset is added to the sensitivities so that they remain positive. The MMA approximation of the compliance at the current design variable a_k is formulated by calculating q_0 and r_0, computed as,

$$q_0 = \left(a_j - L_{kj}\right)^2 \frac{\delta C}{\delta a_j}, r_0 = C - \sum_j \frac{\delta C}{\delta a_j}\left(a_j - L_{kj}\right). \tag{8}$$

Where L_k represents the lower asymptotes at iteration k. Then, the dual problem is solved iteratively by the bisection method to find the optimal value of the dual variable λ. The dual objective function is calculated as,

$$\varphi(\lambda) = r_0 - \lambda V_{max} + \sum_j \frac{q_0}{a_j^* - L_{kj}} + \lambda \sum_j l_j a_j^*. \tag{9}$$

Where a_j are the trial values of the design variable, computed as,

$$a_j^* = L_{kj} + \sqrt{\frac{q_0}{\lambda l_j}}. \tag{10}$$

Once the optimal dual variable λ is found, the design variables are updated as,

$$a_j^{new} = clip(L_{kj} + \sqrt{\frac{q_0}{\lambda l_j}}, a_{max}). \tag{11}$$

The lower asymptotes L_k are also updated for the next iteration,

$$L_k^{new} = L_k + \mu\left(a_j^{new} - L_k\right). \tag{12}$$

The process is repeated until convergence is achieved, i.e., when the change in the design variables between iterations falls below a user-specified tolerance.

2.4. Infill Extruder Path Generation

The generation of machine files for manufacturing objects with topology infill is carried out in two parts: generating the outer shell and generating topology-optimized infill.

First, the design STL model is used to construct the part's outer shell. Commercial slicer software (e.g., Ultimaker Cura and Prusa Slicer) is well-established and can provide error-free shell G-code, so the task of generating shell, top, and bottom surfaces, as well as supports, can be easily implemented by slicers without extra programming. The shell G-code is generated with zero percent infill, resulting in a hollow internal volume.

The infill layers are generated separately using two STL files: the FEA STL model, which is the trimmed lattice structure, including the shell, the same model used for FEA analysis, and the FEA shell STL model, which is the shell of the FEA STL model only. The G-code for the infill layers is inserted at the corresponding layer heights within the G-code for the shell.

2.4.1. Generating Infill via Rasterization

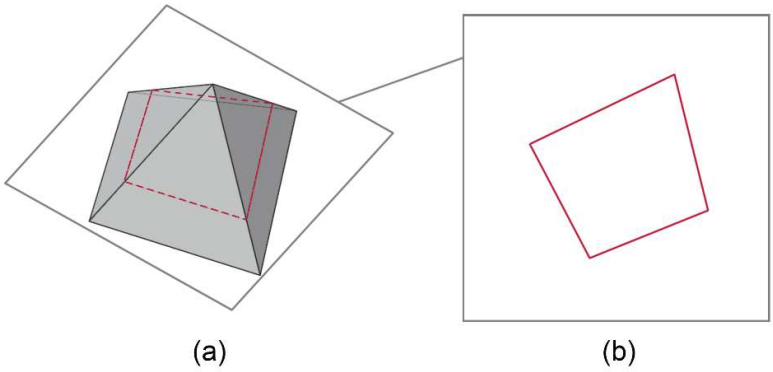


Fig. 8. (a) A geometry cut by a cutting plane and (b) the sliced geometry from the cutting plane.

The FEA mesh defines the shape of the topology-optimized infill. First, the scanning line/plane algorithm searches for triangles of the FEA mesh STL file intersecting the slicing plane. For a valid intersecting triangle, the line segment created by the intersection of the triangle with the plane is calculated using triangle-plane intersection [59-61]. The resulting line segments from all intersecting triangles collectively define the cross-section or slice at that layer, as shown in Figure 8.

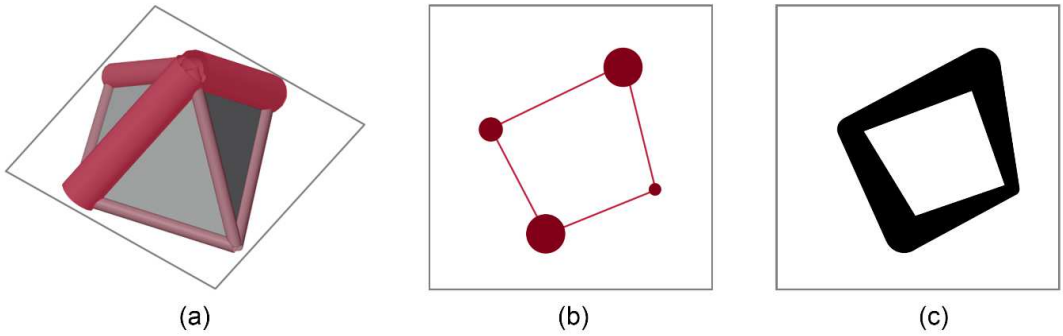


Fig. 9. (a) Geometry showing the struts with topology optimized strut thickness, (b) the sliced geometry overlaid with the corresponding strut thickness, (c) bitmap generated by rasterization.

Unlike the design STL model, the FEA mesh is not a closed, watertight model and has zero volume. As a result, extruder paths for infill cannot be directly produced from the slice. Instead, a rasterization approach is used to define the topology-optimized infill at each layer. In this approach, the line segments obtained from the triangle-plane intersections are rasterized onto a 2D bitmap where black pixels represent the presence of materials, and white pixels represent void regions. It is important to note that for each line segment generated by the triangle-plane intersection, only two edges of the triangle will contribute vertices to the line segment. These two edges are associated with two members and their thicknesses from the parametric definition of the mesh. The thickness obtained after TO is used to define the thickness of the rasterized line created from the intersections. Since each line is assigned two distinct thickness values corresponding to the two edges, it is subdivided into segments with constant Euclidean distance to interpolate the thickness between endpoints. Lastly, a rounded “cap” is added on the endpoints of each line. The rasterization process is shown in Figure 9. The method can be easily modified to generate a conventional open-cell lattice by simply rasterizing circles at the points of intersection, rather than rasterizing lines in between.

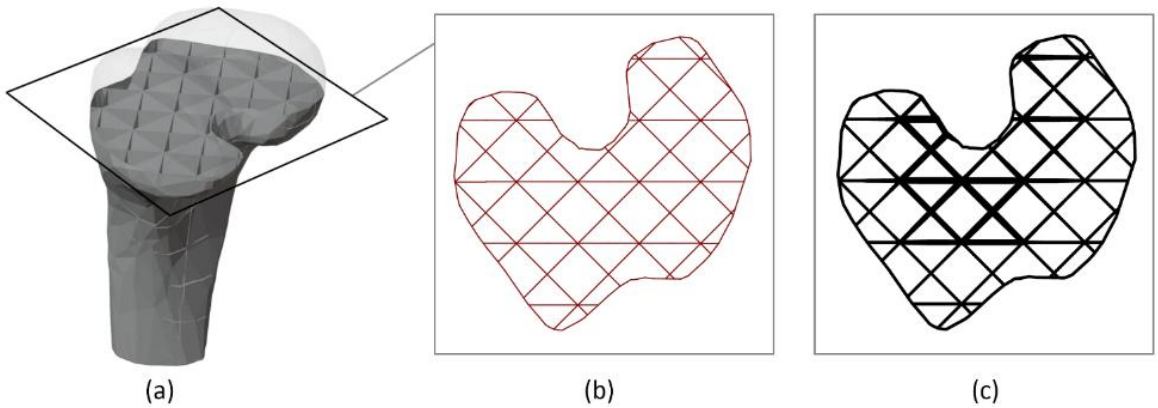


Fig. 10. (a) Femur geometry cut by cutting plane, (b) the sliced geometry from the cutting plane, (c) Bitmap generated by rasterization of sliced geometry.

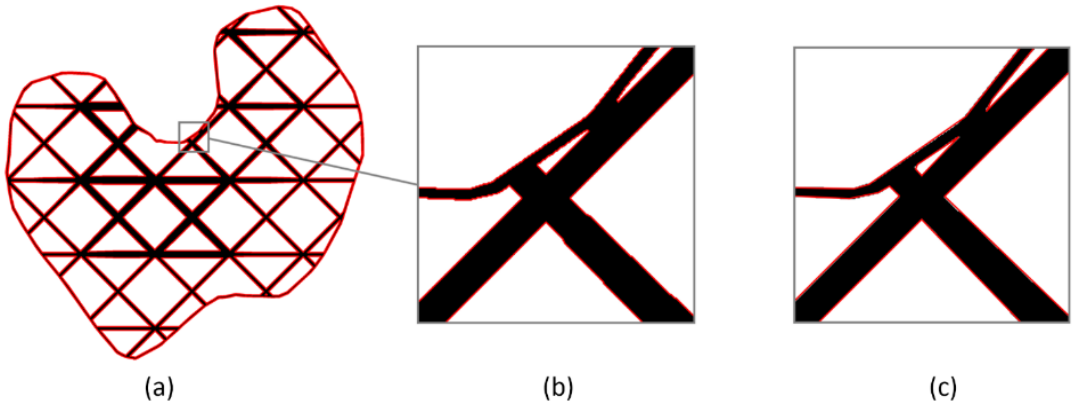


Fig. 11. (a) Contour extraction from bitmap using the marching squares algorithm, (b) contour extracted, (c) contour after the Ramer-Douglas-Peucker algorithm.

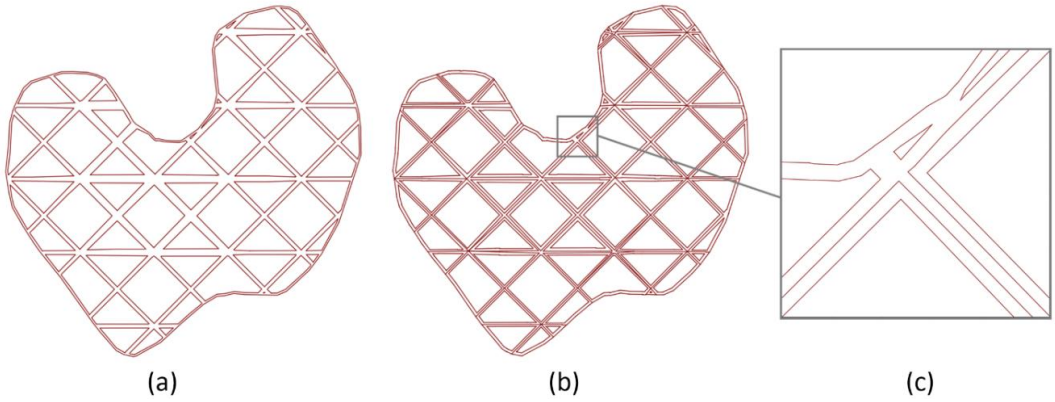


Fig. 12. (a) Contour extracted from bitmap, (b) Offset paths generated inside contour, (c) Contour following offset paths.

Since the shell is also included in the FEA mesh, and the line is rasterized along the middle of the intersection line, the rasterization will also generate materials along the perimeter that extend outside the FEA mesh. To prevent the infill from interfering with the shell when being printed, all the pixels outside the contour of the shell are set as white pixels, so that material is not deposited in those regions. For 3D cases, the contour is obtained by slicing the shell STL, whereas for 2D cases, the contour is obtained by identifying the edges in the STL file that are not shared by more than one triangle.

2.4.2. Generating Extruder Paths from Bitmap

The output of rasterization is a bitmap that defines the layer-wise presence of material, as shown in Figure 10. For some AM processes that use raster slices (e.g., Stereolithography), the bitmaps are directly suited for writing the machine files required. However, to make it suitable for FDM, the bitmap must be translated into paths the extruder can follow. A possible route for FDM manufacturing is to convert the bitmap to an STL file, slice the geometry, and generate the G-code. However, the number of facets required to define the object makes this computationally intensive-slicing software cannot always cope with the high-poly STL file, and it is difficult to achieve highly refined details. So, in this case, the extruder paths and the subsequent G-code are generated directly from the bitmaps.

To convert the bitmap to extruder paths, the contours are traced from the bitmap using the Marching Squares Algorithm, which is a 2D computer graphics algorithm that generates contours from a scalar field or binary image (e.g., a bitmap) [62]. However, due to the discrete nature of bitmaps, the contours generated by the marching square algorithm are dense and jagged. Thus, contour extraction is followed by the line simplification method- Ramer-Douglas-Peucker (RDP) algorithm, which is used to simplify and smooth the polygon. As shown in Figure 12, RDP reduces the number of vertices while preserving sharp corners.

Unlike conventional infill patterns, which consist of individual extruded filaments [63], topology-optimized infill may be thick solid areas. In this case, the inner regions of solid areas are filled with material by generating contour-filling paths, as shown in Figure 12. Thus, the segments produced from contour extraction must be organized into closed, ordered polygons, and the interior polygons – polygons fully contained inside other polygons – are identified. This is required because subsequent processes require the computation of offset polygons, such as to compensate

for the extrusion width, generate multiple perimeters, and set the direction of the offset [64]. The Shapely library was used, which can generate a clean and self-intersection-free offset of complex polygons.

2.4.3. G-code Generation

The proposed method focuses on the direct G-code generation of the topology-optimized infill; however, it does not function as a fully standalone slicer, and a conventional slicer is used to generate the outer walls and the top and bottom surfaces, as shown in Figure 13. The complex computation associated with these features is best delegated to well-established slicer software, allowing the method to focus on infill generation, which is the primary contribution of this work.

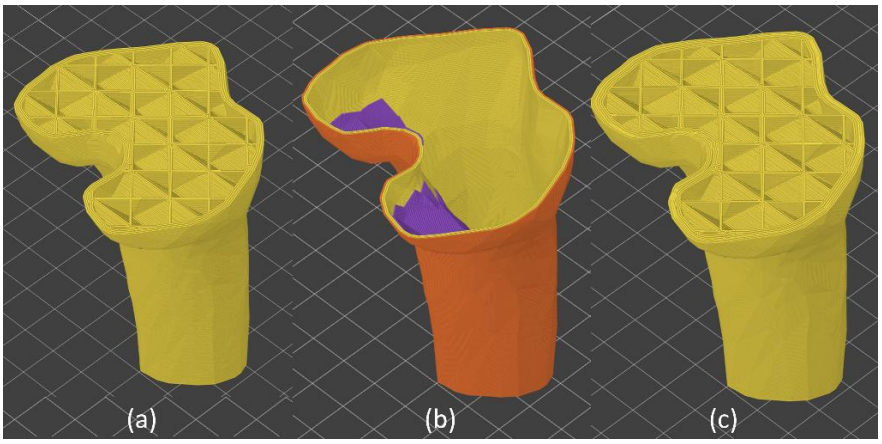


Figure 13. Visualization of the G-code and combining process: (a) topology-optimized infill toolpaths generated by the proposed method, (b) shell toolpaths (outer walls and top/bottom surfaces) generated using PrusaSlicer, and (c) combined G-code showing the combined shell and topology-optimized infill toolpath.

In summary, the proposed framework generates only the topology-optimized infill toolpaths by direct G-code generation from rasterized FEA slices, whereas all shell-related features, including outer walls, top and bottom surfaces, are generated entirely by a commercial slicer (PrusaSlicer). To combine the two toolpaths, the program reads the shell G-code generated by the slicer and inserts the topology-optimized infill G-code at the corresponding Z-height. The infill is appended after the shell toolpaths of each layer, effectively a “infill after wall” mode of printing, which is the default in most Slicers.

Since the coordinates of the extruder paths are defined by the position of the pixels in the bitmap, the resultant paths are multiplied by a scaling factor to convert to millimeter units. The scaling factor depends on the size of the bitmap image and the actual measurements of the object.

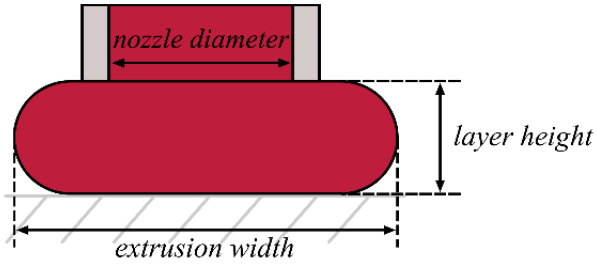


Fig. 14. Extrusion profile.

In FDM 3D printing, each extruded line is associated with an extrusion value, E, which is the amount of material pushed through the extruder. The value is calculated based on the Euclidean distance between the previous and new points, as well as the extrusion profile of the deposited material. In this case, the extrusion profile is assumed to be capsule-shaped [65, 66], as shown in Figure 14.

Using a conventional slicer in conjunction with the proposed infill generation method introduces some practical constraints. For proper alignment, the spatial position of the design STL on the build plate must match that of all the STL files associated with infill. Moreover, the printing parameters, such as layer height, extrusion width, must be consistent with the slicer settings. The inserted G-code also inherits the motion parameters (acceleration, jerk) from the slicer. which cannot be specifically optimized for the infill. Additionally, due to differences between the 3D surface offsets used in FEA mesh generation and those calculated by the slicer to create the walls, the interface between the shell and infill is not always parallel, which can result in small overlaps or gaps between the toolpaths.

3. Results and Discussion

The method has been tested for both 2D and 3D cases. It was implemented using Python and run on a PC with an AMD Ryzen 7 5700X 8-Core Processor, NVIDIA GeForce RTX 3060, and 16 GB of RAM. The computing time for the TO stage ranges from 5 to 10 seconds for 2D cases with approximately 3,000 nodes, and from 30 to 50 seconds for 3D cases with approximately 12,000

nodes. Generally, the computing time for the g-code generation stage—which includes slicing, rasterization, processing, and g-code generation—is 5 to 10 seconds per layer. The objects shown in this study were printed using an Any Cubic Kobra 3D printer at an extruder temperature of 205 °C, a velocity of 60 mm/s, a layer height of 0.2 mm, and with white PLA material supplied by SUNLU. In general, the topology-optimized parts take 30-40% longer to print than their uniform infill counterparts. The tests are conducted on a universal testing machine (UTM) set to provide a constant linear displacement of 2 mm/min, and the displacement continues until the specimen fails.

3.1. Computational Experiments

3.1.1. Uniform 2D Beam

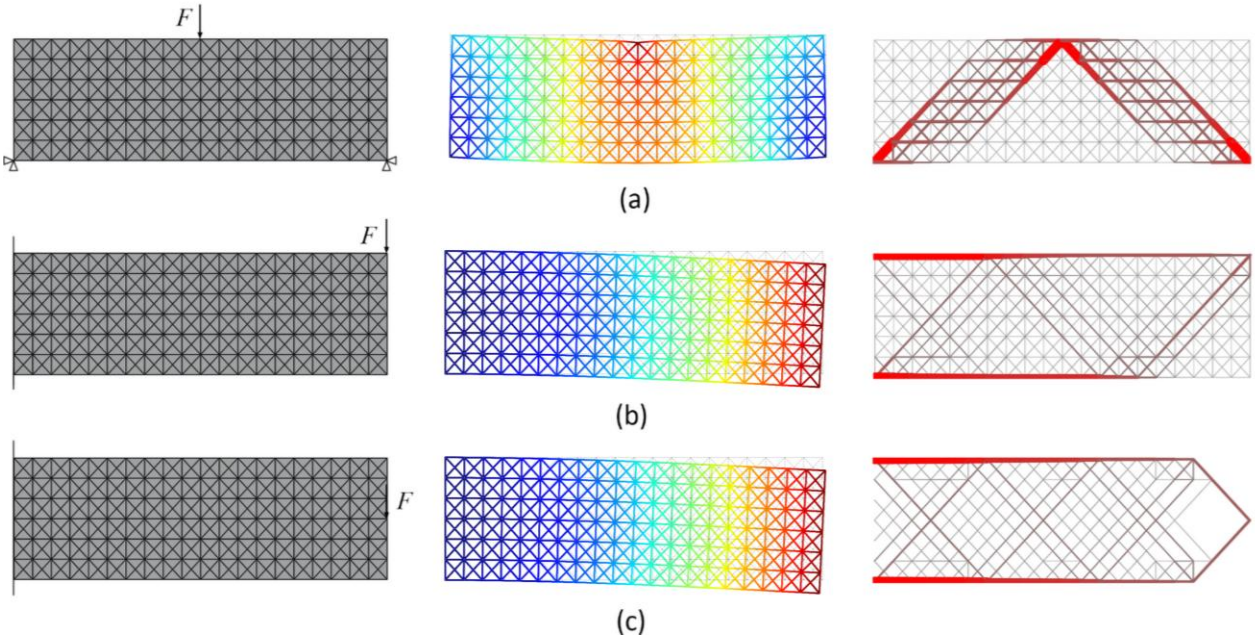


Fig. 15. Boundary conditions and initial lattice configurations (left), displacement for the initial structure (middle), and topology-optimized lattice structures (right) with strut thickness indicated in red. (a) MBB beam with bottom corner nodes fixed and force applied to the middle top node; (b) top-loaded cantilever beam with force applied to the top right node; and (c) center-loaded cantilever beam with force applied to the middle right node.

The method is tested for both 2D and 3D design domains. The first 2D example is a beam with a regular domain that has dimensions of 60×200mm and is composed of 6×20-unit cells. For all cases, the applied force is F = 100 N. The unit cell is a cross-braced square element, where the diagonal members are connected at the point of intersection. Previous literature has mentioned the

advantages of such structures [67]. Different boundary and loading conditions, and the corresponding topology-optimized structure are given in Figure 15. The minimum allowable strut thickness (a_{min}) is 0.4 mm, and the target volume fraction is 0.4.

Figure 16 shows the compliance and the volume fraction throughout the optimization process. The optimization process is stable, where the compliance decreases sharply in the first 10 iterations and converges to the final solution after 250 iterations. For the MBB beam (case a), top-loaded cantilever (case b), and center load cantilever (case c), initial peak displacements were calculated at 0.122 mm, 2.14 mm, and 2.09 mm, respectively. Post-optimization, these values were reduced to 0.04 mm, 0.71 mm, and 0.68 mm. The resultant optimized structure satisfies the target volume fraction and is consistent with the results from previous studies [8, 20].

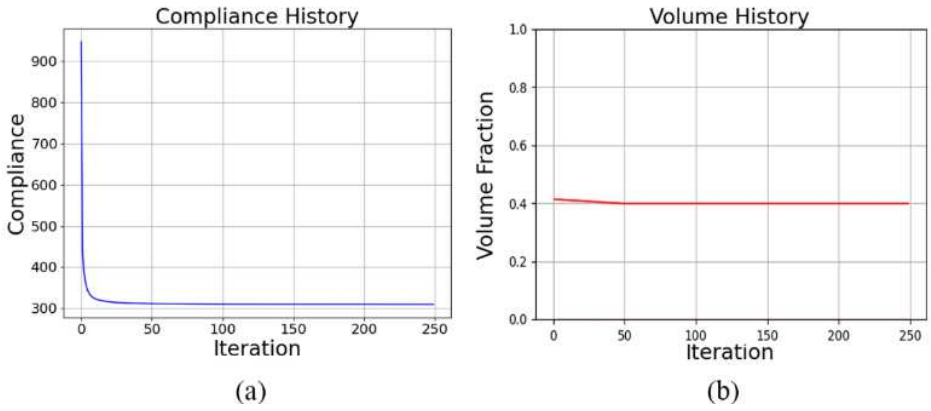


Fig. 16. (a) Compliance vs. iteration, and (b) Volume vs. iteration.

3.1.2. Triangular Mounting Bracket

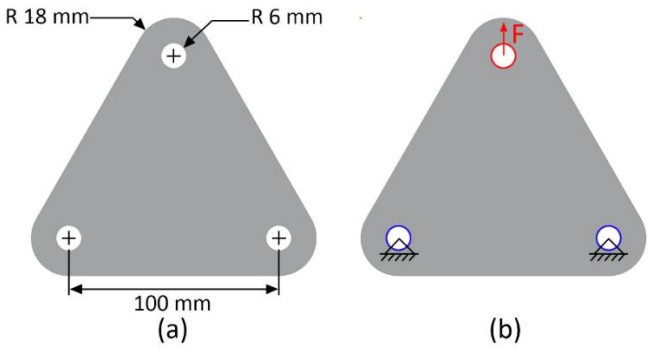


Figure 17. (a) dimensions and (b) boundary and loading conditions of the triangular mounting bracket.

The second 2D example is a free-form object – a triangular mounting bracket of thickness 10 mm. The boundary, loading conditions, and dimensions are given in Figure 17. For this object, all the nodes at the two holes at the bottom are fixed in both axes, and a vertical force F = (0, 0, 100) N is applied to all the nodes at the hole at the top. The minimum allowable strut thickness (a_{min}) is 0.4 mm, and the target volume fraction is 0.4.

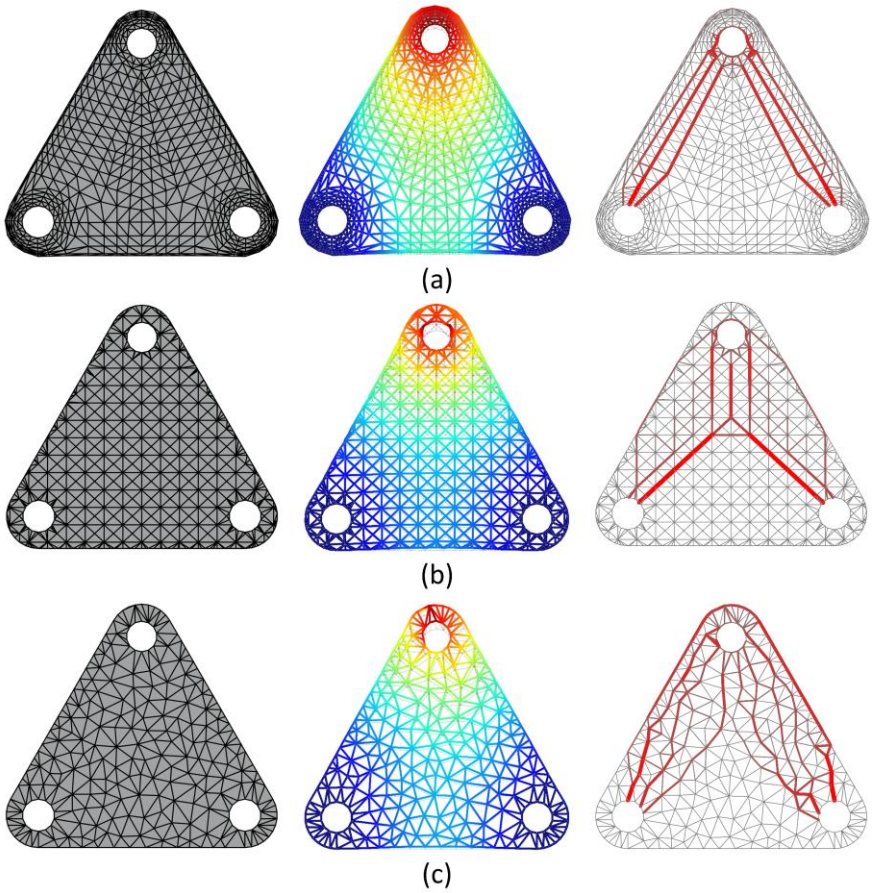


Fig. 18. Initial lattice configurations (left), the displacement for the initial structure (middle), and topology-optimized lattice structures (right) with strut thickness indicated in red. Lattice generated with the methods: (a) meshed, (b) swept, and (c) trimmed.

In this case, three different meshing techniques are used: meshed, swept, and trimmed. The meshed lattice structure was generated using meshing of ANSYS by the tetrahedron patch conforming method. The swept structure is created by first generating quad unit cells along the outer edges, then filling the inner volume with similarly sized quad unit cells. The trimmed lattice was created by generating a 20×20 lattice structure, consisting of cross-braced square unit cells, and trimming it by a Boolean intersection operation. All mesh generation is followed by Delaunay triangulation. It should be noted that the optimized structure obtained through GSM-based optimization depends on the underlying ground structure. The meshes, their deformation, and the corresponding topology-optimized lattice structures are shown in Figure 18. Despite symmetric loading conditions, since symmetry was not enforced during the ANSYS mesh generation, the resulting optimized structure also exhibits asymmetry. Exploiting symmetry in the ground structure may

improve performance, but this was not considered in the present study. For the swept (case a), trimmed (case b), and meshed (case c), initial peak displacements were calculated at 0.281 mm, 0.162 mm, and 0.388 mm, respectively. Post-optimization, these values were reduced to 0.079 mm, 0.046 mm, and 0.110 mm. The resultant optimized structure satisfies the target volume fraction.

Regardless of the shape of the object and the meshing techniques used, the method can generate topology-optimized lattice structures that conform to the exterior of the object.

3.1.3. Uniform 3D Beam

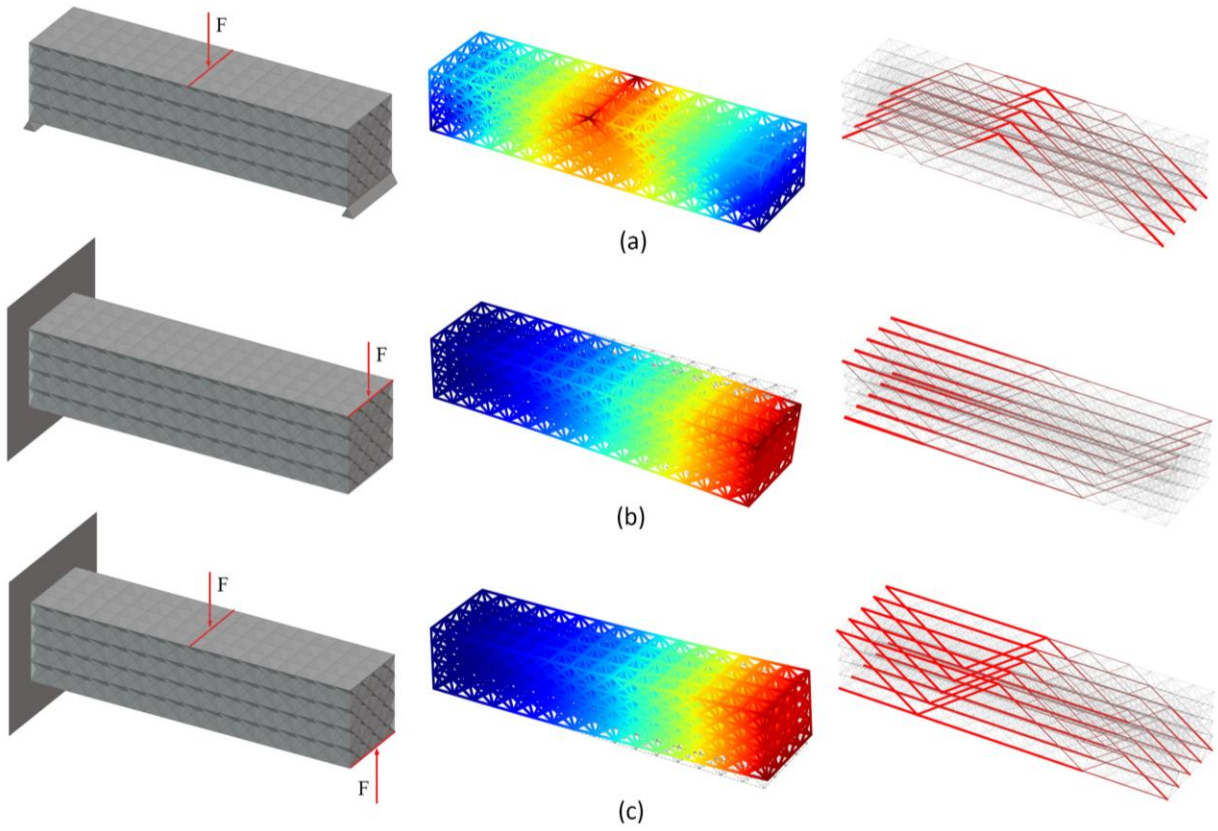


Fig. 19. Boundary conditions and initial lattice configurations (left), the displacement for the initial structure (middle), and topology-optimized lattice structures (right) with strut thickness indicated in red. (a) Messerschmitt-Bölkow-Blohm (MBB) beam (b) Cantilever beam with force applied to the top right edge (c) Cantilever beam with force applied to the middle and bottom right edge.

Similarly, the method is tested for 3D cases with regular and freeform shapes. The first 3D example is a beam with a regular domain that has dimensions of 40×160×40 mm and is composed of

5×20×5-unit cells. The minimum allowable strut thickness (a_{min}) is 0.4 mm, and the target volume fraction is 0.4. Different boundary and loading conditions, and the corresponding topology-optimized structure are given in Figure 19. For the MBB beam (case a), top-loaded cantilever (case b), and middle and bottom loaded cantilever (case c), initial peak displacements were calculated at 0.087 mm, 0.960 mm, and 0.462 mm, respectively. Post-optimization, these values were reduced to 0.03 mm, 0.24 mm, and 0.115 mm. The resultant optimized structure satisfies the target volume fraction and is consistent with the results from previous studies [8, 20].

Figure 20 presents the rasterization results at different layers for the Messerschmitt–Bölkow–Blohm (MBB) beam shown in Figure 19(a). The results show that the infill is adaptively tailored to the stress distribution at each layer.

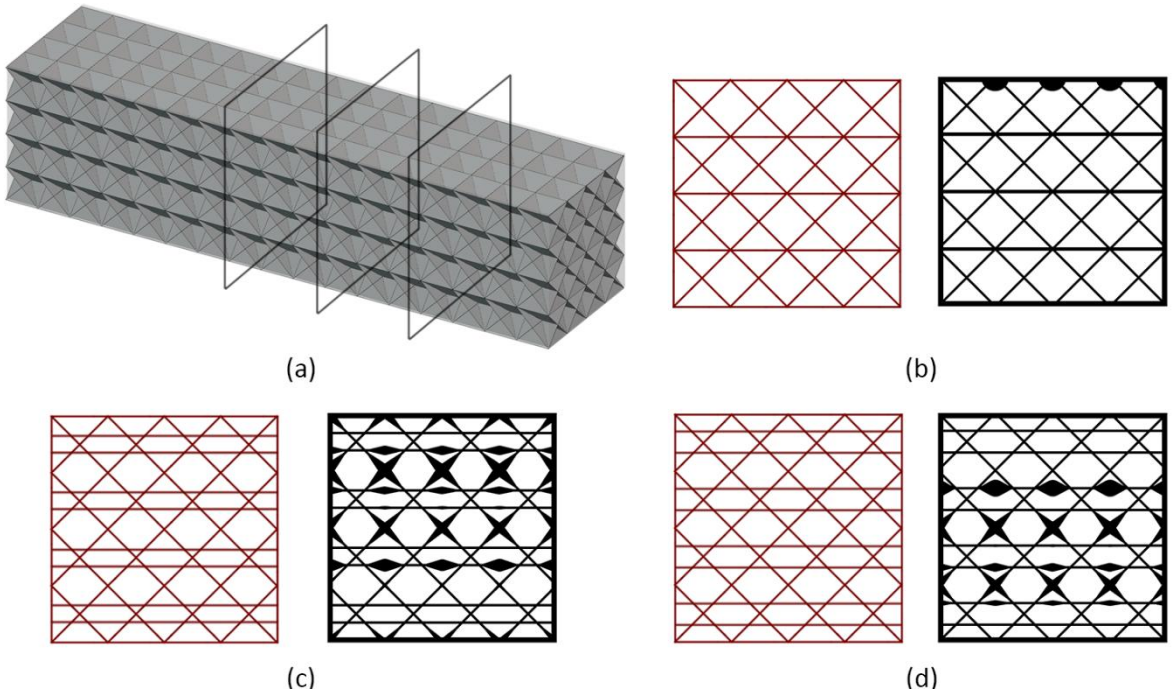


Fig. 20. An MBB beam with internal lattice structure and the cutting planes at layer 801, 1069, and 1336 out of 1601 are shown. The contours are shown at the left, and the corresponding rasterized bitmap for the topology-optimized infill is shown at the right for layer (b) 801, (c) 1069, and (d) 1336.

3.1.4. Human Femur

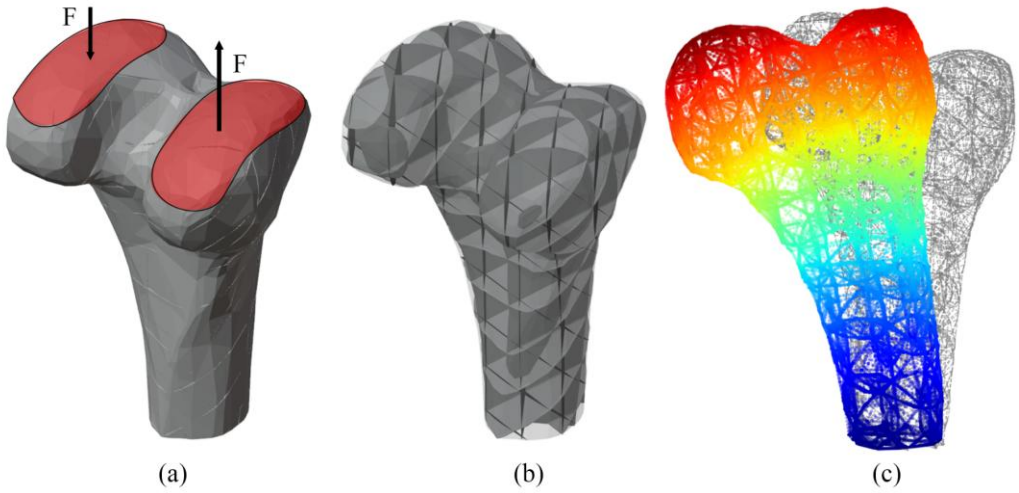


Fig. 21. (a) The forces applied to the femur model, (b) the internal lattice structure, and (c) the exaggerated displacement for the initial structure.

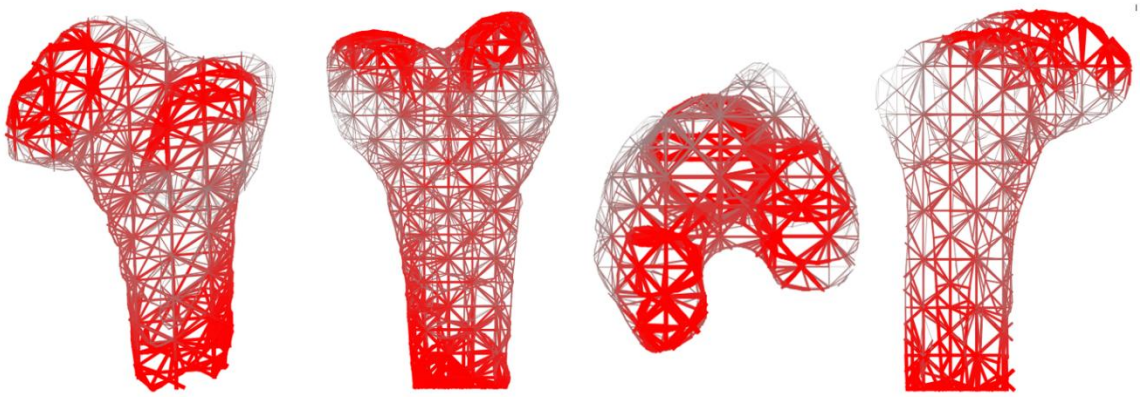


Fig. 22. The result of the topology optimization of the lattice structure viewed from different angles.

The second 3D example is a freeform object – the bottom section of a human femur model, the Distal Epiphysis. The model has overall dimensions of 60×100×60 mm, and the size of the initial lattice structure from which the design volume is trimmed is 12 × 20 × 12 unit cells, as shown in Figure 21. All the nodes at the bottom surface are fixed, and a vertical upward force and a downward force are applied on the top surface. The minimum allowable strut thickness (a_{min}) is 0.4 mm, and the target volume fraction is 0.4. The resultant optimized structure satisfies the target volume fraction and is shown in Figure 22. Figure 23 shows the rasterized 2D bitmap at various layers. The method can generate infill in complex contours, as seen in layer 1055, where there are

convex contours, and is also applicable to layers with multiple isolated patches in the cross-section, as seen in layer 1215.

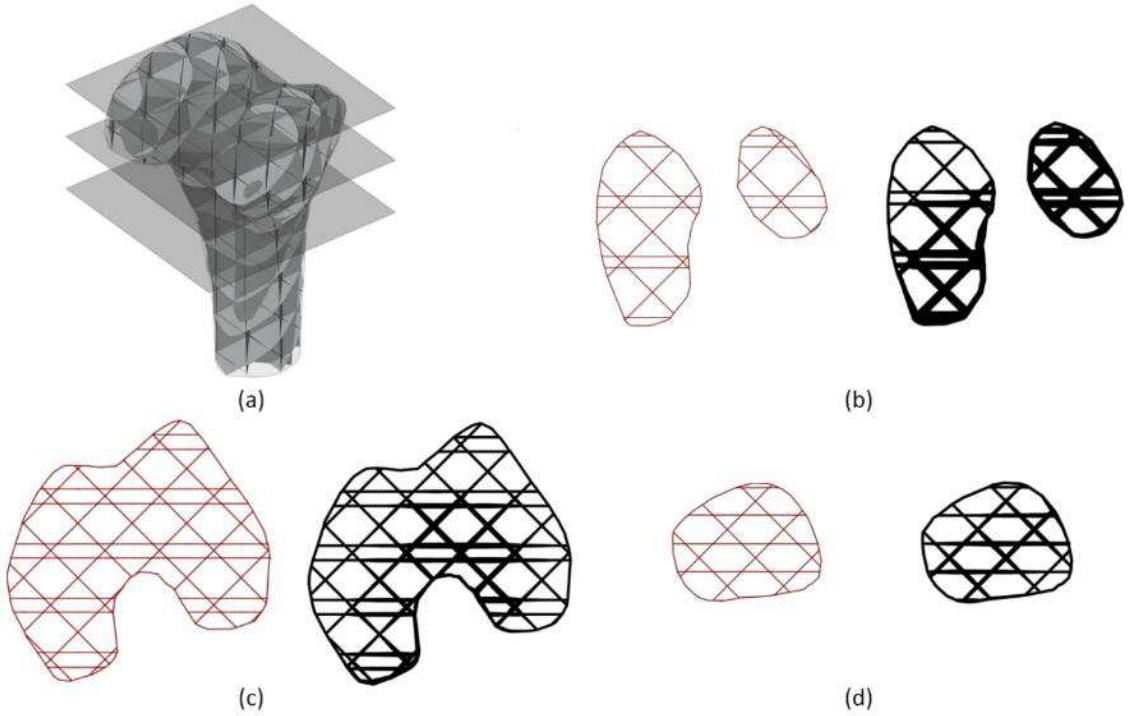


Fig. 23. A beam with internal lattice structure and the cutting planes at layer 575, 1055, and 1215 out of 1307 are shown. The contours are shown at the left, and the corresponding rasterized bitmap for the topology-optimized infill is shown at the right for layer (b) 1215, (c) 1055, and (d) 575.

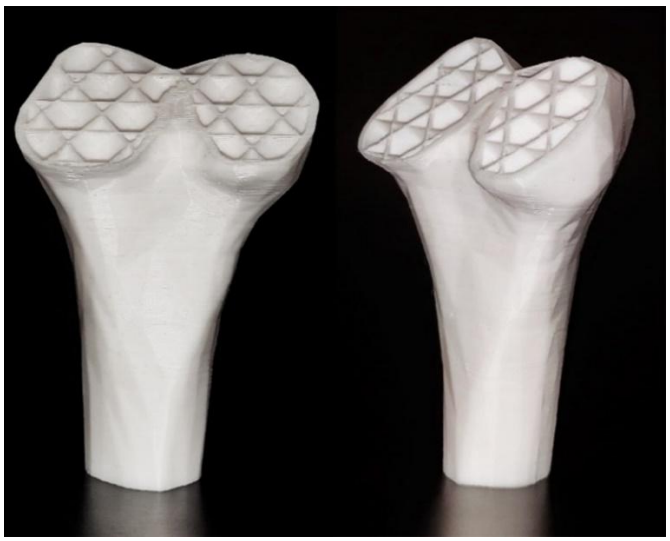


Fig. 24. 3D-printed human femur model with an exposed section to show the topology-optimized infill.

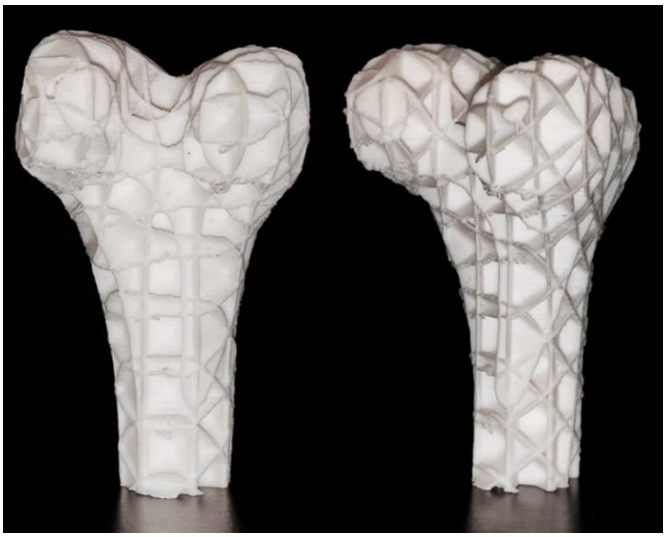


Fig. 25. 3D-printed human femur model with a topology-optimized infill structure only.

The femur model, with 1307 layers, was also printed using the parameters discussed previously. As shown in Figure 24, our method can successfully generate a printable optimized infill structure of the femur model. Moreover, as seen in Figure 25, the femur was also printed with the topology-optimized infill only, without the exterior shell. In this case, both the infill lattice structure and the shell are considered in the optimization. However, the edges common to the FEA shell are not incorporated in the rasterization.

3.2. Experimental Validation and Discussion

3.2.1. Triangular Mounting Bracket

The first case study is a triangular mounting plate, where lattice structures were generated using three different meshing techniques: swept, meshed, and trimmed. The structures were fabricated based on the TO results presented in Section 3.1.2. The topology-optimized structures are generated using a volume fraction of 0.4, using strut dimensions a_{min} = 0.4 mm and a_{max} = 10 mm. For comparison, each topology-optimized part was evaluated against the same structure with uniform infill, with the weight of all the parts maintained at approximately 56 g (±2%) by controlling the line thickness (a_{min} and a_{max} values). The printed triangular brackets are shown in Figure 26, and the UTM setup is shown in Figure 27.

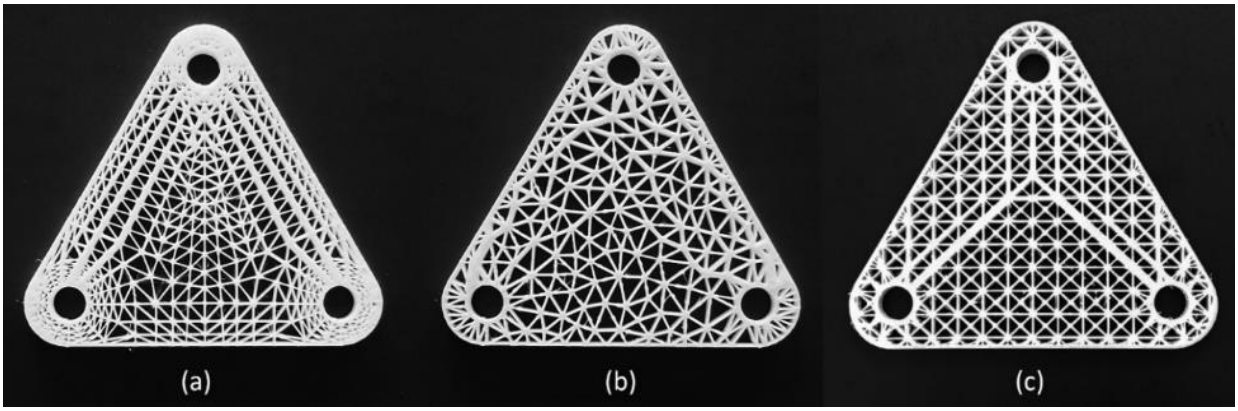


Fig. 26. Printed mounting brackets using mesh generation methods: a) swept, b) meshed, c) trimmed.

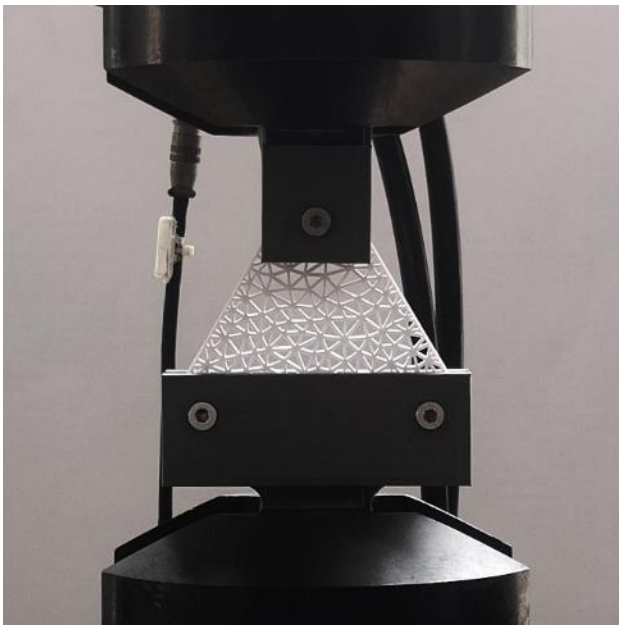


Fig. 27. Mounting bracket UTM testing setup.

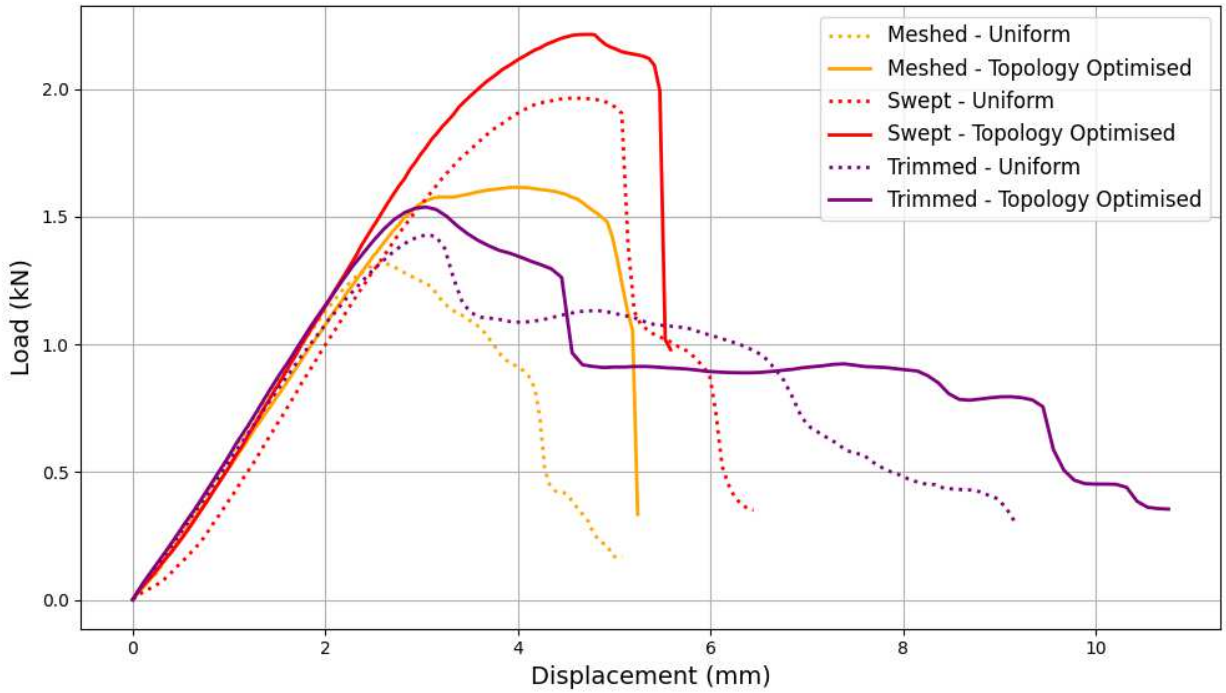


Fig. 28. Load-displacement curve for experimental validation of the mounting plate.

As seen in the results from Figure 28, across all meshing strategies—meshed, swept, and trimmed—the topology-optimized structures demonstrate higher maximum load capacity and greater overall stiffness than their uniform counterparts. The swept topology optimized structure shows the highest peak load and maintains load over a larger displacement. This is consistent with previous studies that state that swept lattice structures show better mechanical properties due to alignment of struts towards the principal stress directions [68-70].

3.2.2. Messerschmitt-Bölkow-Blohm Beam

In the second example, the method is evaluated on a 3D Messerschmitt-Bölkow-Blohm (MBB) beam, where the bottom two edges are fixed, and a vertical force is applied at the top center. The beam has dimensions of 40×160×40 mm and is composed of 5×20×5-unit cells. The topology-optimized structures are generated using a volume fraction of 0.4, using strut dimensions a_{min} = 0.4 mm and a_{max} = 10 mm. The topology-optimized truss is shown in Figure 19(a). In this case, the beam was sliced along the three principal planes, and the planes and the corresponding layers at various midplanes are shown in Figure 29. It is seen that each cutting plane captures the TO differently. The slices along the XY cutting plane give larger infill areas compared to others.

Additionally, the infill pattern differs due to the use of an unsymmetric unit cell. Slicing along the YZ and XZ planes produces infill patterns that alternate between triangles and hexagons, whereas slicing along the XY plane results in patterns alternating between squares and rectangles. The cross-sections of the beam printed about the XY axis are shown in Figure 30, demonstrating that the infill is adaptively tailored to the stress distribution at each layer.

The topology-optimized structures are generated using a volume fraction of 40%, using strut dimensions a_{min} = 0.4 mm and a_{max} = 10 mm. For comparison, each topology-optimized part was evaluated against the same structure with uniform infill, with the weight of all the parts maintained at approximately 105 g (±2%) by controlling the line thickness (a_{min} and a_{max} values). The UTM setup is shown in Figure 31.

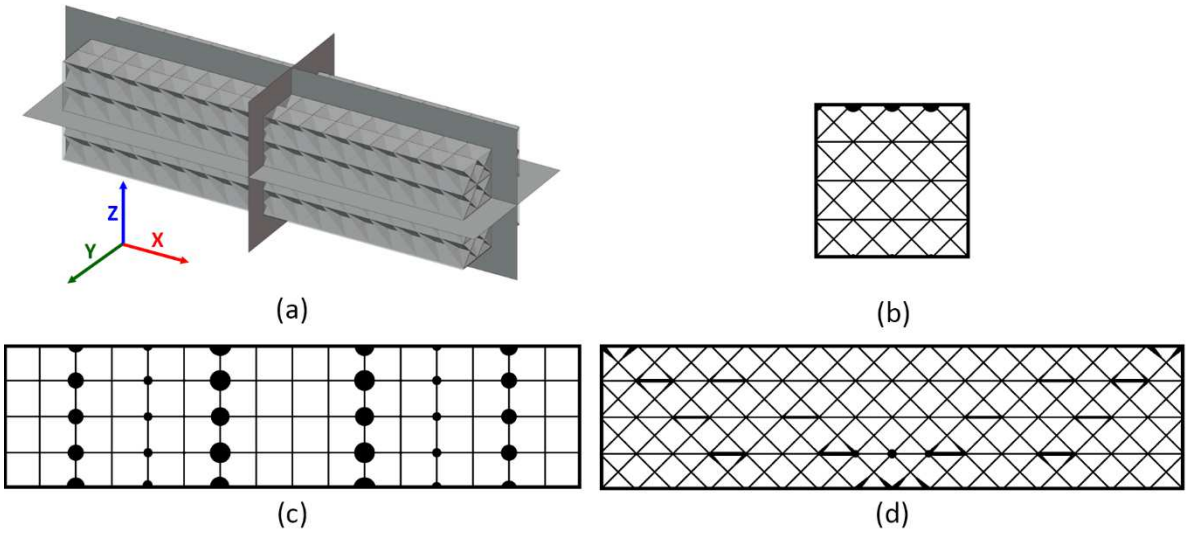


Fig. 29. Lattice structure and various cutting planes about the three principal axes. The output of rasterization at midplanes about the (b) YZ axis, (c) XY axis, and (d) XZ axis.

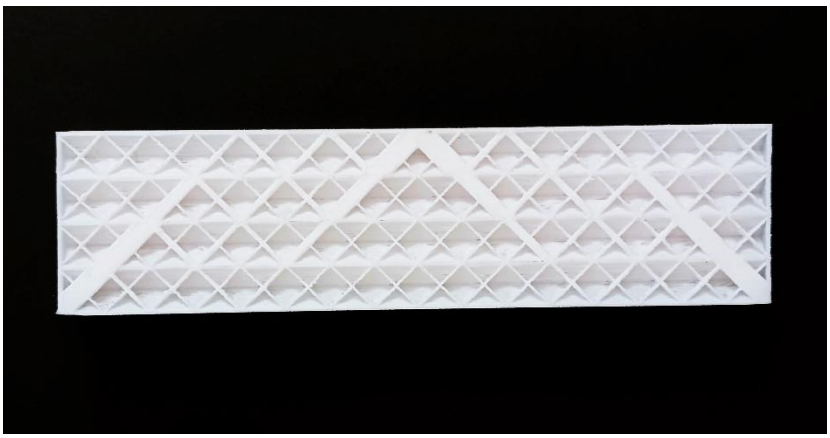


Fig. 30. Cross-section of topology-optimized MBB beam sliced about the XY plane.



Fig. 31. UTM setup.

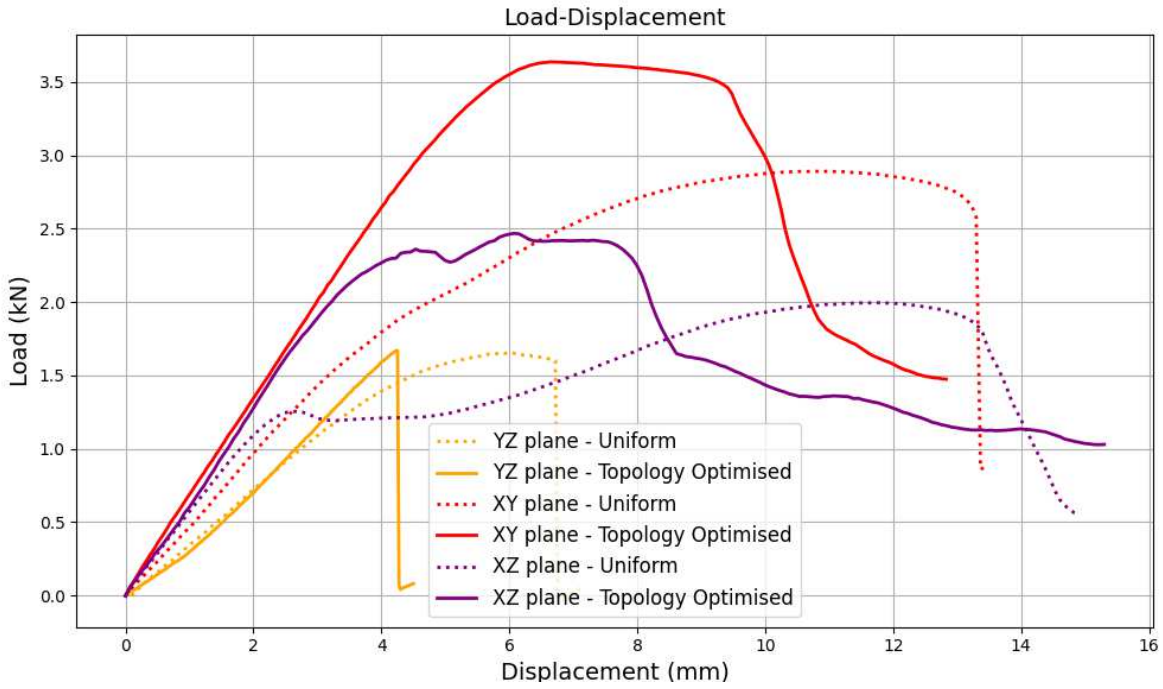


Fig. 32. Load-displacement curve for experimental validation of MBB beam printed along the different principal planes.

As seen in the results from Figure 32, in all the test cases, the topology optimized design consistently outperforms the uniform infill design, exhibiting up to 20 percent higher stiffness, with the maximum gain being achieved during the slicing direction along the XY plane scenario, which is a common characteristic of 3D-printed parts – more stiffness of the part with the alignment of the filament in the principal stress direction [71]. Moreover, this printing orientation experienced the most benefit from TO. The part printed with the slicing direction along the ZY plane shows the lowest rigidity. Notably, this configuration also shows the smallest performance difference between the optimized and uniform infill designs. while the topology-optimized beam shows a stiffer initial response due to a steeper force–displacement curve, the maximum force at failure is nearly the same as that of the uniform infill beam. This shows that co-optimizing the geometry and the print orientation is necessary to take full advantage of our method.

While the numerical simulation of the MBB beam in section 3.1.3(a) predicted a nearly 300% increase in rigidity, the experimental results yielded, at most, a 20% increase. As previously discussed, this performance gap is primarily a consequence of the idealized assumptions inherent to linear-elastic compliance minimization, which assumes ideal material behavior and perfect

inter-layer bonding, rather than accounting for the stochastic and anisotropic nature of FDM printing. Despite the performance gap, the method successfully improved structural performance across all test cases, demonstrating that it can provide mechanical advantages even when constrained by the practical limitations of fused deposition modeling.

Considering the failure modes, it is seen that increasing the stiffness of the beam through TO also increases the brittleness. With the material of the topologized optimized structure concentrated along primary load paths, any failure of an element drastically decreases the load-carrying ability. In contrast, the uniform infill beams begin to plateau at a steady state loading condition. The beam steadily deforms, maintaining the load before failing or reaching a stage where the deforming materials stack on each other to form an almost solid structure. This suggests that while TO is superior for stiffness-critical applications, uniform infill may be preferable for energy absorption requirements.

It is important to note that the shells were also included in these tests, which contribute to the structural rigidity of the printed part. Printing only the infill gave manufacturing defects and made it difficult to mount and apply loads to the specimen. Otherwise, the relative increase in rigidity due to TO would have been greater.

A limitation of the current experimental study is the use of a single specimen per configuration. So, the results do not account for print-to-print variability or stochastic defects such as localized poor layer adhesion and filament diameter fluctuations. While the results demonstrate performance trends, they lack the statistical characterization to define absolute mean performance or standard deviation.

4. Conclusion

In this paper, we present a novel method for producing a topology-optimized infill structure that conforms to any arbitrary 2D and 3D geometry. The method uses the ground-structure approach for optimization, in which the closed-cell shell-lattice infill is modelled as a pin-jointed truss. This modeling approach effectively captures primary load paths and material distribution. While this simplification does not account for the higher bending and shear stiffness inherent in closed-cell lattices, the experimental results indicate that the comparative performance trends remain representative of the design objectives.

A rasterization process is used to represent the topology-optimized infill at each layer from which the machine files were directly created, without generating an intermediate STL file. Multiple mesh generation types were examined for 2D cases, while the trimming method for lattice generation was examined for the 3D case.

The process was experimentally evaluated on both 2D and 3D examples. In the 2D case, the test specimen was a non-uniform mounting plate, with its mesh generated using three different techniques: trimmed, swept, and FEA-based meshing. For the 3D case, an MBB beam was considered, sliced about the 3 principal planes. These tests confirmed a performance increase of the topology-optimized structures. Topology-optimized infill structures consistently outperformed their uniform-infill counterparts, showing higher stiffness and maximum loading capacity while maintaining the same weight. For 2D cases, the results showed the effect of meshing techniques, with the swept mesh structure demonstrating the best performance. For the 3D case, an orientation-dependent behavior was presented, with optimized structures showing the most benefit when the filament is aligned with the principal stress paths. Failure modes also differed—while uniform infill deformed gradually, optimized structures exhibited more brittle behavior. All experimental results were obtained using a single specimen for each configuration. So, the conclusion should be interpreted as demonstrating performance trends rather than statistically characterized improvements. The extension of this method to a wider range of geometries, materials, and printing systems will be explored in future work.

The current program uses an individual node-based boundary condition assignment interface, which is well-suited for small- to medium-scale models. For large-scale problems (more than 12,000 nodes), we found that semi-automating the boundary condition assignment would improve scalability. Implementing a graphical interface is a straightforward extension of the existing workflow, allowing us to handle models with a more detailed design domain and a denser lattice structure without requiring fundamental changes to the core GSM and rasterization algorithms.

Declarations

Funding Statement

No funding was received to assist with the preparation of this manuscript.

Author Contribution Statement

Shadman Tajwar Shahid: Conceived and designed the experiments; Analyzed and interpreted the data; Wrote the paper.
Md. Mahidul Alam: Performed the experiments; Prepared the specimens.
Mahmudul Hasan: Performed the experiments; Wrote the paper.
Md. Rakidul Islam: Performed the experiments; Prepared the specimens; Wrote the paper.
Shah Md. Ahasan Siddique: Prepared the specimens; Contributed materials and tools.

Declaration of Interest Statement

The authors have no relevant financial or nonfinancial interests to disclose.

Ethics Approval and Consent to Participate

Not applicable.

Data Availability Statement

Data associated with this study are available at https://doi.org/10.5281/zenodo.16923073.

Replication of Results: The G-code files for the test cases (triangular mounting bracket, MBB beam, and femur model) are available at https://doi.org/10.5281/zenodo.16923073.

References

1. Iftekar, S. F., Aabid, A., Amir, A., & Baig, M. (2023). Advancements and Limitations in 3D Printing Materials and Technologies: A Critical Review. Polymers 2023, Vol. 15, Page 2519, 15(11), 2519. https://doi.org/10.3390/POLYM15112519
2. Gibson, I., Rosen, D., Stucker, B., & Khorasani, M. (2020). Additive manufacturing technologies. Additive Manufacturing Technologies, 1–675. https://doi.org/10.1007/978-3-030-56127-7/COVER
3. Dolenc, A., & Mäkelä, I. (1994). Slicing procedures for layered manufacturing techniques. Computer-Aided Design, 26(2), 119–126. https://doi.org/10.1016/0010-4485(94)90032-9

4. Kedziora, S., Decker, T., & Museyibov, E. (2023). Application of Functionally Graded Shell Lattice as Infill in Additive Manufacturing. Materials, 16(12). https://doi.org/10.3390/MA16124401
5. Arunkumar, P., Balaji, D., Radhika, N., Rajeshkumar, L., Mavinkere Rangappa, S., & Siengchin, S. (2025). Effect of infill pattern on mechanical properties of 3D printed PLA-Zn composites for drone frame structures: A topology optimization integrated application study. Results in Engineering, 25. https://doi.org/10.1016/J.RINENG.2025.104107
6. Barclift, Michael & Williams, Christopher. (2012). Examining variability in the mechanical properties of parts manufactured via polyjet direct 3D printing. 23rd Annual International Solid Freeform Fabrication Symposium - An Additive Manufacturing Conference, SFF 2012.
7. Suteja, J. (2021). Effect of Infill Pattern, Infill Density, and Infill Angle on the Printing Time and Filament Length of 3D Printing. Jurnal Rekayasa Mesin, 12(1), 145. https://doi.org/10.21776/UB.JRM.2021.012.01.16
8. Liu, Y., Zhou, M., Wei, C., & Lin, Z. (2021). Topology optimization of self-supporting infill structures. Structural and Multidisciplinary Optimization, 63(5), 2289–2304. https://doi.org/10.1007/S00158-020-02805-Y/FIGURES/16
9. Gopsill, J. A., Shindler, J., & Hicks, B. J. (2018). Using finite element analysis to influence the infill design of fused deposition modelled parts. Progress in Additive Manufacturing, 3(3), 145–163. https://doi.org/10.1007/S40964-017-0034-Y
10. Sigmund, O., & Maute, K. (2013). Topology optimization approaches: A comparative review. Structural and Multidisciplinary Optimization, 48(6), 1031–1055. https://doi.org/10.1007/S00158-013-0978-6/METRICS
11. el Khadiri, I., Zemzami, M., Nguyen, N. Q., Abouelmajd, M., Hmina, N., & Belhouideg, S. (2023). Topology optimization methods for additive manufacturing: a review. International Journal for Simulation and Multidisciplinary Design Optimization, 14, 12. https://doi.org/10.1051/SMDO/2023015
12. ZHU, J., ZHOU, H., WANG, C., ZHOU, L., YUAN, S., & ZHANG, W. (2021). A review of topology optimization for additive manufacturing: Status and challenges. Chinese Journal of Aeronautics, 34(1), 91–110. https://doi.org/10.1016/J.CJA.2020.09.020
13. Pan, C., Han, Y., & Lu, J. (2020). Design and Optimization of Lattice Structures: A Review. Applied Sciences 2020, Vol. 10, Page 6374, 10(18), 6374. https://doi.org/10.3390/APP10186374
14. Clausen, A., Aage, N., & Sigmund, O. (2016). Exploiting Additive Manufacturing Infill in Topology Optimization for Improved Buckling Load. Engineering, 2(2), 250–257. https://doi.org/10.1016/J.ENG.2016.02.006

15. Siva Rama Krishna, L., Mahesh, N., & Sateesh, N. (2017). Topology optimization using solid isotropic material with penalization technique for additive manufacturing. Materials Today: Proceedings, 4(2), 1414–1422. https://doi.org/10.1016/J.MATPR.2017.01.163
16. Panesar, A., Abdi, M., Hickman, D., & Ashcroft, I. (2018). Strategies for functionally graded lattice structures derived using topology optimisation for Additive Manufacturing. Additive Manufacturing, 19, 81–94. https://doi.org/10.1016/J.ADDMA.2017.11.008
17. Alzahrani, M. A., Choi, S.-K., & Rosen, D. W. (2014). Design of Truss-Like Cellular Structures Using the Relative Density Mapping Method. https://doi.org/10.1115/DETC2014-34566
18. Aremu, A. O., Brennan-Craddock, J. P. J., Panesar, A., Ashcroft, I. A., Hague, R. J. M., Wildman, R. D., & Tuck, C. (2017). A voxel-based method of constructing and skinning conformal and functionally graded lattice structures suitable for additive manufacturing. Additive Manufacturing, 13, 1–13. https://doi.org/10.1016/J.ADDMA.2016.10.006
19. Xiao, X., & Cirak, F. (2021). Infill topology and shape optimisation of lattice-skin structures. International Journal for Numerical Methods in Engineering, 123(3), 664–682. https://doi.org/10.1002/nme.6866
20. Wang, W., Feng, D., Yang, L., Li, S., & Wang, C. C. L. (2023). Topology optimization of self-supporting lattice structure. Additive Manufacturing, 67, 103507. https://doi.org/10.1016/J.ADDMA.2023.103507
21. Liu, F., Chen, M., Wang, L., Luo, T., & Chen, G. (2023). Stress-field driven conformal lattice design using circle packing algorithm. Heliyon, 9(3), e14448. https://doi.org/10.1016/J.HELIYON.2023.E14448
22. McMillan, M., Jurg, M., Leary, M., & Brandt, M. (2015). Programmatic Lattice Generation for Additive Manufacture. Procedia Technology, 20, 178–184. https://doi.org/10.1016/J.PROTCY.2015.07.029
23. Kim, J. E., & Park, K. (2021). Multiscale Topology Optimization Combining Density-Based Optimization and Lattice Enhancement for Additive Manufacturing. International Journal of Precision Engineering and Manufacturing - Green Technology, 8(4), 1197–1208. https://doi.org/10.1007/S40684-020-00289-1/METRICS
24. Chen, W., Zheng, X., & Liu, S. (2018). Finite-element-mesh based method for modeling and optimization of lattice structures for additive manufacturing. Materials, 11(11). https://doi.org/10.3390/MA11112073
25. Wu, Z., Xia, L., Wang, S., & Shi, T. (2019). Topology optimization of hierarchical lattice structures with substructuring. Computer Methods in Applied Mechanics and Engineering, 345, 602–617. https://doi.org/10.1016/j.cma.2018.11.003

26. Rodrigues, H., Guedes, J. M., & Bendsoe, M. P. (2002). Hierarchical optimization of material and structure. Structural and Multidisciplinary Optimization, 24(1), 1–10. https://doi.org/10.1007/S00158-002-0209-Z/METRICS
27. Coelho, P. G., Fernandes, P. R., Guedes, J. M., & Rodrigues, H. C. (2008). A hierarchical model for concurrent material and topology optimisation of three-dimensional structures. Structural and Multidisciplinary Optimization, 35(2), 107–115. https://doi.org/10.1007/S00158-007-0141-3/METRICS
28. Wang, C., Zhu, J. H., Zhang, W. H., Li, S. Y., & Kong, J. (2018). Concurrent topology optimization design of structures and non-uniform parameterized lattice microstructures. Structural and Multidisciplinary Optimization, 58(1), 35–50. https://doi.org/10.1007/s00158-018-2009-0
29. Wang, Y., Xu, H., & Pasini, D. (2017). Multiscale isogeometric topology optimization for lattice materials. Computer Methods in Applied Mechanics and Engineering, 316, 568–585. https://doi.org/10.1016/j.cma.2016.08.015
30. Dong, G., Tang, Y., Li, D., & Zhao, Y. F. (2020). Design and optimization of solid lattice hybrid structures fabricated by additive manufacturing. Additive Manufacturing, 33, 101116. https://doi.org/10.1016/J.ADDMA.2020.101116
31. Tang, Y., Kurtz, A., & Zhao, Y. F. (2015). Bidirectional Evolutionary Structural Optimization (BESO) based design method for lattice structure to be fabricated by additive manufacturing. CAD Computer Aided Design, 69, 91–101. https://doi.org/10.1016/j.cad.2015.06.001
32. Cheng, L., Zhang, P., Biyikli, E., Bai, J., Robbins, J., & To, A. (2017). Efficient design optimization of variable-density cellular structures for additive manufacturing: Theory and experimental validation. Rapid Prototyping Journal, 23(4), 660–677. https://doi.org/10.1108/RPJ-04-2016-0069
33. Ranalli, Filippo & Flager, Forest & Fischer, Martin. (2018). A Ground Structure Method to Minimize the Total Installed Cost of Steel Frame Structures.
34. Zhao, T., & Paulino, G. H. (n.d.). AN IMPLEMENTATION OF THE GROUND STRUCTURE METHOD CONSIDERING BUCKLING AND NODAL INSTABILITIES.
35. Dorn, W., Gomory, R., & Greenberg, H. J. (1964). Automatic design of optimal structures.
36. Chen, W., Zheng, X., & Liu, S. (2018). Finite-Element-Mesh Based Method for Modeling and Optimization of Lattice Structures for Additive Manufacturing. Materials 2018, Vol. 11, Page 2073, 11(11), 2073. https://doi.org/10.3390/MA11112073

37. Ohsaki, M., & Hayashi, K. (2017). Force density method for simultaneous optimization of geometry and topology of trusses. Structural and Multidisciplinary Optimization, 56(5), 1157–1168. https://doi.org/10.1007/s00158-017-1710-8
38. Hayashi, K., & Ohsaki, M. (2019). FDMopt: Force density method for optimal geometry and topology of trusses. Advances in Engineering Software, 133, 12–19. https://doi.org/10.1016/j.advengsoft.2019.04.002
39. Huang, Y., Carstensen, J. v, & Mueller, C. T. (n.d.). 3D truss topology optimization for automated robotic spatial extrusion.
40. Zegard, T., & Paulino, G. H. (2015). GRAND3 — Ground structure based topology optimization for arbitrary 3D domains using MATLAB. Structural and Multidisciplinary Optimization, 52(6), 1161–1184. https://doi.org/10.1007/S00158-015-1284-2/FIGURES/34
41. Zienkiewicz, O. C., Taylor, R. L., & Govindjee, S. (2024). The Finite Element Method: Its Basis and Fundamentals, Eighth Edition. The Finite Element Method: Its Basis and Fundamentals, Eighth Edition, 1–613. https://doi.org/10.1016/C2022-0-01494-X
42. Lumpe, T. S., & Shea, K. (2021). Computational design of 3D-printed active lattice structures for reversible shape morphing. Journal of Materials Research, 36(18), 3642–3655. https://doi.org/10.1557/S43578-021-00225-2
43. Nazir, A., Waqar, S., ul Haq, M. R., & Tanveer, M. Q. (2024). Design for additive manufacturing of cellular structures. Additive Manufacturing Materials and Technology, 359–388. https://doi.org/10.1016/B978-0-443-18462-8.00014-3
44. Lo, S. H. (2002). Finite element mesh generation and adaptive meshing. Progress in Structural Engineering and Materials, 4(4), 381–399. https://doi.org/10.1002/PSE.135
45. Beyer, C., & Figueroa, D. (2016). Design and Analysis of Lattice Structures for Additive Manufacturing. Journal of Manufacturing Science and Engineering, Transactions of the ASME, 138(12). https://doi.org/10.1115/1.4033957
46. Alwattar, T. A., & Mian, A. (2019). Development of an elastic material model for bcc lattice cell structures using finite element analysis and neural networks approaches. Journal of Composites Science, 3(2). https://doi.org/10.3390/JCS3020033
47. Huang, Y., Zha, W., Xue, Y., & Shi, Z. (2021). Compressive behaviour of aluminium pyramidal lattice material-filled tubes. Materials, 14(14). https://doi.org/10.3390/MA14143817
48. McMillan, M., Jurg, M., Leary, M., & Brandt, M. (2015). Programmatic Lattice Generation for Additive Manufacture. Procedia Technology, 20, 178–184. https://doi.org/10.1016/J.PROTCY.2015.07.029

49. de la Rosa, S., Mayuet Ares, P. F., & Rodríguez-Parada, L. (2025). Design of Flexible TPU-Based Lattice Structures for 3D Printing: A Comparative Analysis of Open-Cell Versus Closed-Cell Topologies. Polymers, 17(9). https://doi.org/10.3390/POLYM17091133
50. Han, D., Yang, F., Li, P., Li, P., Li, L., Bai, C., Fan, H., & Ren, X. (2025). Design, fabrication and mechanical properties of a new cylindrical lattice metamaterial. Thin-Walled Structures, 213. https://doi.org/10.1016/J.TWS.2025.113292
51. Yavas, D., Liu, Q., Zhang, Z., & Wu, D. (2022). Design and fabrication of architected multi-material lattices with tunable stiffness, strength, and energy absorption. Materials & Design, 217, 110613. https://doi.org/10.1016/J.MATDES.2022.110613
52. Park, S. I., Rosen, D. W., Choi, S. kyum, & Duty, C. E. (2014). Effective mechanical properties of lattice material fabricated by material extrusion additive manufacturing. Additive Manufacturing, 1, 12–23. https://doi.org/10.1016/J.ADDMA.2014.07.002
53. Xu, W., Liu, Y., Yu, M., Wang, D., Hou, S., Li, B., Wang, W., & Liu, L. (2022). A Support-Free Infill Structure Based on Layer Construction for 3D Printing. IEEE Transactions on Visualization and Computer Graphics, 28(12), 4462–4476. https://doi.org/10.1109/TVCG.2021.3091509
54. Koc, B., & Lee, Y. S. (2002). Non-uniform offsetting and hollowing objects by using biarcs fitting for rapid prototyping processes. Computers in Industry, 47(1), 1–23. https://doi.org/10.1016/S0166-3615(01)00141-5
55. Roylance, D. (2001). Finite Element Analysis. http://ocw.mit.edu/courses/materials-science-and-engineering/3-11-mechanics-of-materials-fall-1999/modules/
56. Christensen, P. W., & Klarbring, A. (2008). An introduction to structural optimization. Solid Mechanics and Its Applications, 153, 1–220. https://doi.org/10.1007/978-1-4020-8666-3_1
57. Bendsøe, M. P., & Sigmund, O. (2004). Topology Optimization. Topology Optimization. https://doi.org/10.1007/978-3-662-05086-6
58. Taylor, J. E., & Rossow, M. P. (n.d.). OPTIMAL TRUSS DESIGN BASED ON AN ALGORITHM USING ~PTIMALITY CRITERIA.
59. Zhang, Z., & Joshi, S. (2015). An improved slicing algorithm with efficient contour construction using STL files. International Journal of Advanced Manufacturing Technology, 80(5–8), 1347–1362. https://doi.org/10.1007/S00170-015-7071-9
60. Sunday, Daniel. (2021). Practical geometry algorithms with C++ code. 185. https://dokumen.pub/practical-geometry-algorithms-with-c-code-9798749449730.html
61. Schurig, F. (n.d.). Slicing Algorithms for 3D-Printing.
62. Eck, D. J. (n.d.). Introduction to Computer Graphics ©2015-2023, David J. Eck. Retrieved July 28, 2025, from http://math.hws.edu/graphicsbook

63. Gleadall, A., Ashcroft, I., & Segal, J. (2018). VOLCO: A predictive model for 3D printed microarchitecture. Additive Manufacturing, 21, 605–618. https://doi.org/10.1016/J.ADDMA.2018.04.004
64. Nguyen, X. A., King, P., Vargas-Uscategui, A., Lohr, H., & Chu, C. (2023). A continuous toolpath strategy from offset contours for robotic additive manufacturing. Journal of the Brazilian Society of Mechanical Sciences and Engineering, 45(12), 1–10. https://doi.org/10.1007/S40430-023-04544-9/FIGURES/6
65. Foteinopoulos, P., Esnault, V., Komineas, G., Papacharalampopoulos, A., & Stavropoulos, P. (2020). Cement-based additive manufacturing: experimental investigation of process quality. International Journal of Advanced Manufacturing Technology, 106(11–12), 4815–4826. https://doi.org/10.1007/S00170-020-04978-8/TABLES/13
66. Tao, Y., Li, P., & Pan, L. (2020). Improving tensile properties of polylactic acid parts by adjusting printing parameters of open source 3D printers. Medziagotyra, 26(1), 83–87. https://doi.org/10.5755/J01.MS.26.1.20952
67. Kemp, A. R., & Behncke, R. H. (1998). Behavior of Cross-Bracing in Latticed Towers. Journal of Structural Engineering, 124(4), 360–367. https://doi.org/10.1061/(ASCE)0733-9445(1998)124:4(360)
68. Faisal, M. F., Akbar, N. I., & Zayed, A. H. H. (2024). Development and Analysis of Additively Manufactured Non-Pneumatic Tires for Mars Rover. IOP Conference Series: Materials Science and Engineering, 1305(1), 012026. https://doi.org/10.1088/1757-899X/1305/1/012026
69. Wang, H., Chen, Y., & Rosen, D. W. (2005). A hybrid geometric modeling method for large scale conformal cellular structures. Proceedings of the ASME International Design Engineering Technical Conferences and Computers and Information in Engineering Conference - DETC2005, 3 A, 421–427. https://doi.org/10.1115/DETC2005-85366
70. Nguyen, J., Park, S. in, & Rosen, D. (2013). Heuristic optimization method for cellular structure design of light weight components. International Journal of Precision Engineering and Manufacturing, 14(6), 1071–1078. https://doi.org/10.1007/S12541-013-0144-5/METRICS
71. Farzadi, A., Solati-Hashjin, M., Asadi-Eydivand, M., & Osman, N. A. A. (2014). Effect of Layer Thickness and Printing Orientation on Mechanical Properties and Dimensional Accuracy of 3D Printed Porous Samples for Bone Tissue Engineering. PLOS ONE, 9(9), e108252. https://doi.org/10.1371/JOURNAL.PONE.0108252